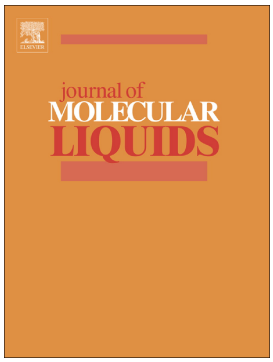

Synthesis of magnetic CMC bionanocomposite containing a novel biodegradable nanoporous polyamide selectively synthesized in ionic liquid as green media: Investigation on Nd+3, Tb+3, and Dy+3 rare earths adsorption

Hamedreza Javadian, Montserrat Ruiz, Mehdi Taghavi, Ana Maria Sastre

PII: S0167-7322(19)35950-1

DOI: https://doi.org/10.1016/j.molliq.2020.113017

Reference: MOLLIQ 113017

To appear in: *Journal of Molecular Liquids*

Received date: 27 October 2019

Revised date: 20 March 2020

Accepted date: 28 March 2020

Please cite this article as: H. Javadian, M. Ruiz, M. Taghavi, et al., Synthesis of magnetic CMC bionanocomposite containing a novel biodegradable nanoporous polyamide selectively synthesized in ionic liquid as green media: Investigation on Nd+3, Tb+3, and Dy+3 rare earths adsorption, *Journal of Molecular Liquids* (2018), https://doi.org/10.1016/j.molliq.2020.113017

Synthesis of magnetic CMC bionanocomposite containing a novel biodegradable nanoporous polyamide selectively synthesized in ionic liquid as green media: Investigation on Nd^{+3}, Tb^{+3}, and Dy^{+3} rare earths adsorption

Hamedreza Javadian[a,*], Montserrat Ruiz[b], Mehdi Taghavi[c], Ana Maria Sastre[a]

[a]Department of Chemical Engineering, ETSEIB, Universitat Politècnica de Catalunya, Diagonal 647, 08028 Barcelona, Spain

[b]Department of Chemical Engineering, EPSEVG, Universitat Politècnica de Catalunya, Av. Víctor Balaguer, s/n, 08800 Vilanova i la Geltrú, Spain

[c]Department of Chemistry, Faculty of Science, Shahid Chamran University of Ahvaz, 61357-43337, Iran

[*]Corresponding author.

Email addresses: Hamedreza.javadian@yahoo.com; Hamedreza.javadian@upc.edu

Abstract

In this research study, the carboxymethyl chitosan/poly(pyrimidine-thiophene-amide)/ $Ni_{0.2}Zn_{0.2}Fe_{2.6}O_4$ (CMC/P(PTA)/$Ni_{0.2}Zn_{0.2}Fe_{2.6}O_4$) was prepared as a novel magnetic bionanocomposite adsorbent. FE-SEM, EDX, NMR, XRD, FT-IR, and VSM techniques were applied for the analyses of the products. The adsorption behavior of the prepared bionanocomposite was investigated towards Nd^{+3}, Tb^{+3}, and Dy^{+3} as adsorbates. The adsorption process was evaluated considering the influence of independent parameters including pH of the solution, contact time, adsorbent dosage, initial metal ions concentration, and ionic strength. The adsorption efficiency values of 98.15, 97.6, and 99.42 % were respectively obtained for Nd^{+3}, Tb^{+3}, and Dy^{+3} at optimum conditions of pH = 5.5, 30 mg/L of the ions, adsorbent dosage of 0.06 g, and contact time of 90 min. The data of the adsorption equilibrium of the ions were fitted well by Freundlich model. Kinetic studies showed that Nd^{+3}, Tb^{+3}, and Dy^{+3} adsorption followed both pseudo-second-order (PSO) and intra-particle diffusion (IPD) kinetic models. The values of ΔH° indicated that the ions adsorption process onto the bionanocomposite was endothermic, and the ΔG° values revealed that it was spontaneous at higher temperature. The CMC/P(PTA)/$Ni_{0.2}Zn_{0.2}Fe_{2.6}O_4$ could be regenerated by 0.2 M HNO_3 and its separation was viable utilizing a magnetic field with the saturation magnetization value of 14.88 emu/g.

Keywords: Carboxymethyl chitosan, Poly(pyrimidine-thiophene-amide), Magnetic, Bionanocomposite, Adsorption, Rare earth elements.

1. Introduction

Rare Earth Elements (REEs) contain 17 components of the periodic table that include 15 lanthanides together with yttrium and scandium [1-3]. Light and heavy REEs are the additional subdivision of REEs based on atomic number. They possess exceptional properties and are regularly named as "seeds of technology" [4]. They are extensively utilized in various fields, for example, electronics, metallurgy, catalysis, alloys, superconductors, lasers, fertilizers, chemical reagents, nuclear energy, and magnets [5,6]. The total demand for REEs was reported 128,000 tons in 2011, and this amount was raised up to 170,000 tons in 2015. It is also anticipated that it would increase up to 255,000 tons in 2020 with around 6-10 %/year growth rate [7]. This anticipated large demand for REEs is as a result of their broad usage in numerous fields of human life. According to this matter, their recovery from wastes seems to be necessary. Different techniques, such as precipitation, ion exchange, solvent extraction, and adsorption have been utilized for REEs recovery from aqueous media [8-11]. Numerous investigations have shown adsorption as a high-efficient, cost-effective and simple technique for REEs recovery from aqueous media amongst the physicochemical treatment techniques.

Chitosan is a derivation of chitin, a natural polysaccharide that comprises β(1-4)- 2-amino-2-deoxy-D-glucan units and possesses superb adsorption performance for metal ions, chiefly owing to containing a large amount of amino and hydroxyl groups [12]. Its structure is like a crystal with hydrogen bonds. Nonetheless, the protonation of the amino groups in the acidic medium leads to losing structural strength by the formation of a gel-like solution that results in significant restrictions of its applications [13]. So as to solve this issue, the modification of chitosan has been carried out by sulfonation, nitration, hydroxyalkylation, quarternarization, hydroxylation, polyethyleneglycol-grafting, carboxymethylation, and so on

[14,15]. Amongst the derivatives of chitosan, carboxymethyl chitosan (CMC) is an amphoteric ether derivative that each molecule comprises the active groups of -COOH, -OH, and -NH_2. The carboxymethylation of chitosan causes it to be dissolved in water. Thus, the problem related to losing the structural stability that takes place by -NH_2 protonation in the acidic medium can be solved [16]. In addition, carboxyl groups are able to increase metal ions adsorption [17]. Whereas chitosan is a natural polymer, its derivatives like CMC also have some advantages such as being biocompatible and low toxic.

Recently, numerous polycondensation reactions have been conducted in ionic liquids (ILs) at room temperature (RT) as a substitute to several volatile toxic solvents [18]. In industry, it is necessary to substitute a great number of organic solvents with environmentally, nonvolatile and green solvents for preparing high molecular weight polymers. The attraction of ambient temperature imidazolium based ILs for substantial commercial productions and applications as solvents and catalysts in polymerization, extraction, and as alternatives for ordinary volatile organic solvents has been confirmed. Reviewing the ILs application in polymer fabrication verifies their performance. Consequently, different processes of polycondensation in the ionic medium have been effectively conducted [19].

In recent years, increasing attention in the studies of synthetic polymer-polymer composites owing to the unique combination of beneficial properties and construction of multifunctional structures of each component has been reported. These composites display potentially greater thermal, mechanical, and electrical properties than the unique polymer [20]. Synthetic PAs are generally known as the first engineering plastics and are still considered as one of the best and most prominent classes of these types of materials. Hence, these polymers introduction in the natural polymers chemical structures is able to supply enhanced properties for

individual usages, for which polymer having these sequences have shown incredibly excellent properties [21].

In this study, CMC, a novel biodegradable nanoporous polyamide (poly(pyrimidine-thiophene-amide)) synthesized by polycondensation reaction of 5,5'-(thiophen-2-ylmethylene)bis(2-aminopyrimidine-4,6-diol) (TMAPD) with terephthalic acid in 1,3-dipropyl imidazolium bromide {[1,3-$(pr)_2$im]Br} ionic liquid as green media, and the hydrothermally synthesized $Ni_{0.2}Zn_{0.2}Fe_{2.6}O_4$ were applied to produce a novel bionanocomposite (CMC/P(PTA)/$Ni_{0.2}Zn_{0.2}Fe_{2.6}O_4$) by the gelation process. FE-SEM, EDX, NMR, XRD, FT-IR, and VSM were utilized to confirm the fabrication of the products. In the following, it was used as an adsorbent to investigate its effectiveness for Nd^{+3}, Tb^{+3}, and Dy^{+3} ions adsorption. The influences of different factors including solution pH, contact time, adsorbent dosage, initial metal ions concentration, and ionic strength on the adsorption efficiency were considered. The models of adsorption kinetic and isotherm were employed to reach the best fitting of the experimental data. The reusability of the adsorbent was also investigated.

2. Materials and methods

2.1. Materials and reagents

Carboxymethyl chitosan was purchased from Nantong Chem-Base Co, China. $Dy(NO_3).5H_2O$ was purchased from Alfa Aesar. $Nd(NO_3)_3.6H_2O$, $Tb(NO_3)_3 \cdot 6H_2O$, $Zn(NO_3)_2.6H_2O$, $Fe(NO_3)_3.9H_2O$, $Ni(NO_3)_2 \cdot 6H_2O$, glutaraldehyde, 2-amino-4,6-dihydroxypyrimidine, 2-thiophenecarboxaldehyde, terephthalic acid, triphenyl phosphite (TPP), dimethyl sulfoxide (DMSO), and methanol were bought from Sigma-Aldrich. All chemicals chosen in this study were at analytical grade and were utilized as received without further purification. The experiment solutions of Nd^{+3}, Tb^{+3}, and Dy^{+3} ions were made by the dilution of 1000 mg/L of

ions. To adjust the initial value of pH in the test solutions to the desired value, appropriate molarity of HNO_3 or NaOH was used.

2.2. Instrumentation and characterization

The XRD pattern was recorded by a X-ray diffractometer (GBC MMA), and the samples were scanned from $2\theta = 10^{\circ}$ to 70°. A spectrophotometer (PerkinElmer, USA) was also used to record FT-IR spectra. Bruker Advance DRX was employed to record ^{1}H NMR and ^{13}C NMR spectra at 400 MHz and 100 MHz, respectively, by DMSO-d_6 as a solvent. The nitrogen adsorption-desorption isotherm was measured at −196 °C using a Micromeritics Tristar 3000 apparatus. The morphology of the products was explored by a FE-SEM (Zeiss Neon-40, Germany). TGA measurements were performed by Mettler TGA/SDTA 851e/LF/1100 thermobalance under the atmosphere of N_2 from RT to 1000 °C with a rate of 10 °C/min. Magnetic measurements were done using a vibrating sample magnetometer (VSM, Daghigh Kavir Corporation, Iran). For analyzing the concentration of Nd^{+3}, Tb^{+3}, and Dy^{+3}, an Agilent 4100 MP-AES Spectrometer was used.

2.3. Synthesis of the $Ni_{0.2}Zn_{0.2}Fe_{2.6}O_4$ magnetic nanoparticles

The $Ni_{0.2}Zn_{0.2}Fe_{2.6}O_4$ magnetic nanoparticles were synthesized by the hydrothermal method. A mixed solution of 0.2 M Ni^{2+}, 0.2 M Zn^{2+}, and 2.6 M Fe^{3+} was prepared in HCl solution, and then NaOH solution was added into the mixed solution under nitrogen gas, and the mixture pH value was set to 10.5. 0.3 g of CTAB was added to this mixture, and then it was placed into an autoclave (Teflon-lined stainless steel) at 200 °C of an oven. After 8 h of hydrothermal treatment, the temperature of the autoclave was naturally decreased to RT, and the precipitate was collected and washed several times with deionized water (DW) to reach neutral pH. Finally, the obtained particles were dried at 50 °C.

2.4. Synthesis of the ionic liquid (1,3-dipropyl imidazolium bromide) and the monomer (5,5'-(thiophen-2-ylmethylene)bis(2-aminopyrimidine-4,6-diol (TMAPD))

The RT ionic liquid (IL) was synthesized based on the process presented in the literature [22]. TMAPD was synthesized according to the following procedure: A mixture of 2.54 g (0.02 mol) 2-amino-4,6-dihydroxypyrimidine, 1 mL (0.01 mol) 2-thiophenecarboxaldehyde, and 20 mL DMSO was stirred for 6 h at 110 °C. After completion of the reaction tested by thin-layer chromatography, the temperature of the solution was decreased to RT, and the violet powder obtained by pouring the solution into 400 mL of cold DW (-5 °C) was filtered, rinsed several times using DW and then dried using vacuum oven at 100 °C. The reaction yield was 92 % (3.20 g), and the obtained compound has not shown sharp melting point and started to be decomposed above 300 °C. FT-IR (KBr, cm^{-1}): 3153-3477 (stretching of O-H and NH_2), 3049 (stretching of C-H aromatic), 2944 (stretching of C-H aliphatic), 1651 (stretching of C=N), 1586 (stretching of C=C), 1232 (C-N) and 1163 (C-O). ^{1}H NMR (DMSO-d_6, δ in ppm) (**Fig. 1**): 5.33 (s, 1H, CH), 6.61 (s, 4H, -NH_2), 6.78-6.80 (d, 1H, Ar-H, *J*= 5.6 Hz), 6.93-6.94 (d, 1H, Ar-H, *J*= 5.6 Hz), 7.42-7.44 (d, 1H, Ar-H, *J*= 5.2 Hz), 10.95-11.28 (m, 4H, broad, hydroxy pyrimidine). ^{13}C NMR (100 MHz, (DMSO-d_6, δ in ppm) (**Fig. 2**): 30.98, 115.41, 128.27, 128.55, 137.86, 140.13, 143.76, 170.77.

2.5. Synthesis of the biodegradable nanoporous P(PTA) by polycondensation reaction of TMAPD in TPP/IL

The synthesis of the biodegradable nanoporous P(PTA) was carried out from a compound containing multi polar thiophene, amine, and free hydroxyl chelating groups. It was particularly synthesized from the diamine-phenol compound in 1,3-dipropyl imidazolium bromide as an ionic liquid without using toxic triphenyl phosphite/N-methylpyrolidone/pyridine/LiCl that is needed

in the ordinary direct polycondensation. The P(PTA) was achieved by polycondensation of TMAPD using TPP-IL as catalyst and solvent by the following procedure: A flask of three-necked round-bottomed with the volume of 50 mL was fitted with a mechanical stirrer, a water cooled condenser, and argon gas, and then a mixture containing 1 mmol TMAPD, 1 mmol terephthalic acid, 0.7 g 1,3-dipropyl imidazolium bromide {[1,3-$(pr)_2$im]Br} as IL, and 1.29 mmol TPP was placed. The solution became sticky as the reaction continued at 110 $^{\circ}$C for 2.5 h. In the following, the reaction mixture temperature was decreased to RT and the precipitation of the obtained P(PTA) was performed using 100 mL of methanol. After the precipitate filtration, the hot water was used for washing it. Afterward, the precipitate was further refined in a Soxhlet apparatus using methanol for 24 h to eliminate the oligomers with low molecular weight. FT-IR (KBr, cm^{-1}): 3164-3337 (stretching of O-H and NH_2), 3054 (stretching of C-H aromatic), 2958 (stretching of C-H aliphatic), 1683 (stretching of C=O amide), 1641 (stretching of C=N), 1593 (stretching of C=C), 1215 (C-N) and 1167 (C-O). ^{1}H NMR (DMSO-d_6, δ in ppm) (**Fig. 3**): 5.37 (s, 1H, CH), 7.25-7.27 (m, 2H, Ar-H), 7.44 (s, 1H, Ar-H), 7.99-8.00 (d, 2H, Ar-H, J= 3.2 Hz), 8.06-8.08 (d, 2H, Ar-H, J= 5.2 Hz), 11.01 (s, 1H, OH amide), 11.32 (m, 4H, broad, hydroxy pyrimidine).

2.6. Synthesis of the CMC/P(PTA)/$Ni_{0.2}Zn_{0.2}Fe_{2.6}O_4$ magnetic bionanocomposite

The magnetic bionanocomposite was synthesized by the gelation method. Carboxymethyl chitosan powder was dissolved in dionized water (DW) (3 % w/v) under stirring at 150 rpm for 3 h to prepare carboxymethyl chitosan solution. Then, 0.5 g of the P(PTA) and 0.7 g of the $Ni_{0.2}Zn_{0.2}Fe_{2.6}O_4$ were added to carboxymethyl chitosan solution and fully dispersed with vigorous stirring within 24 h. The gelation process was then performed by adding the mixture to a solution of $CaCl_2$ (0.05 M) and 2 % glutaraldehyde. The mixture was stirred for 24 h, and the

separation of the obtained bionanocomposite was performed using an external magnet. It was washed using deionized water several times to eliminate all impurities (unreacted GA) and remaining calcium chloride and reach the solution pH value of 7. The washed CMC/P(PTA)/$Ni_{0.2}Zn_{0.2}Fe_{2.6}O_4$ bionanocomposite was dried at 50 °C. Finally, it was powdered.

2.7. Adsorption experiments

Nd^{+3}, Tb^{+3}, and Dy^{+3} metal ions adsorption onto the CMC/P(PTA)/$Ni_{0.2}Zn_{0.2}Fe_{2.6}O_4$ was done by batch equilibrium method in aqueous solution at 25 °C. The standard stock solutions of 1000 mg/L of $Nd(NO_3)_3.6H_2O$, $Tb(NO_3)_3 \cdot 6H_2O$, $Dy(NO_3).5H_2O$ ions were prepared. The adsorption experiments were carried out by mixing 0.03 g of the adsorbent with 50 mL of metal ions solutions at 180 rpm and 25 °C. The influence of pH on the adsorption efficiency of the adsorbent was tested between 1.5 and 5.5. The ions adsorption onto the adsorbent was carried out at various time intervals (2.5-120 min) to evaluate adsorption kinetics. The influence of the adsorbent dosage on the adsorption of the ions was carried out from 0.01 to 0.07 g. To study the adsorption isotherms, different initial concentrations of the metal ions (30, 50, 70, 90, 120, 180, 240, and 300 mg/L) were utilized. The ionic strength influence on the adsorption efficiency was also taken into consideration by preparing the solutions with the ionic strengths of 0.02, 0.04, 0.06, 0.08, and 0.1 M using $NaNO_3$. The magnetic adsorbent was separated at the end of each experiment, and the metal ions concentration in the solutions was measured by Agilent 4100 MP-AES Spectrometer. The adsorption efficiency (%) and capacity of adsorption of the metal ions by the CMC/P(PTA)/$Ni_{0.2}Zn_{0.2}Fe_{2.6}O_4$ were calculated based on the bellowing equations:

$$\text{Adsorption efficiency (\%)} = (C_0 - C_e)/C_o \times 100 \quad (1)$$

$$q_e = (C_0 - C_e) \times V/m \quad (2)$$

$$q_t = (C_0 - C_t) \times V/m \quad (3)$$

Where q_e and q_t (mg/g) show the amounts of adsorbed ion at equilibrium and adsorption time t (min), respectively. C_0 and C_e refer to the initial and equilibrium concentrations of metal ion (mg/L), respectively. C_t shows the concentration of metal ion in the solution at time t, V shows the volume of solution (L), and m refers to the weight of the adsorbent (g).

2.8. Reusability studies

The reusability experiments were performed on the CMC/P(PTA)/$Ni_{0.2}Zn_{0.2}Fe_{2.6}O_4$ using adsorption-desorption cycles. A given amount of the bionanocomposite was added into 50 mL solutions of 30 mg/L of each metal ion at an optimum time. After the adsorption process, the obtained metal ions-loaded bionanocomposite was washed several times with DW to eliminate the unreacted metal ions, and then it was added to 0.2 M HNO_3 solution for desorption process at shaking speed = 180 rpm and temperature of 25 °C for 2 h. After ending the process and collecting the adsorbent, the concentration of the ions was measured by Agilent 4100 MP-AES Spectrometer. The adsorption-desorption process was occurred four times using the identical adsorbent.

3. Results and discussion

3.1. Analyses of the products

N_2 adsorption–desorption isotherm and the corresponding Barrett-Joyner-Halenda (BJH) pore size distribution of the P(PTA) are shown in **Fig. 4**. The nitrogen adsorption-desorption isotherm for the sample in **Fig. 4A** is assigned to type IV indicating the presence of mesoporous structure. The Brunauer–Emmett–Teller (BET) surface area, pore volume, and pore size (obtained by the BJH method (**Fig. 4B**)) were calculated to be 6.7420 m^2/g, 0.030884 cm^3/g, and 22.5244 nm, respectively. The results clearly demonstrate the formation of the P(PTA) with nano size pores.

The XRD pattern of the $Ni_{0.2}Zn_{0.2}Fe_{2.6}O_4$ is indicated in **Fig. 5**. The peaks at $2\theta = 18.13^{\circ}$, 30.07°, 35.50°, 37.08°, 43.07°, 53.95°, 56.96°, and 63.89° are in agreement with the standard pattern of nickel zinc ferrite (JCPDS 08-0234) [23]. Full Width at Half Maximum (FWHM) of the XRD pattern strongest reflection was used to estimate the average crystal size via the Scherrer equation as following [24]:

$$D = k\lambda/\beta \cos\theta \quad (4)$$

Where k shows the function of shape (k = 0.89), λ refers to the X-ray wavelength of the radiation, and β presents the Full Width at Half Maximum (FWHM) at $2\theta = 35.50^{\circ}$ and θ shows the diffraction angle. Based on the Scherrer equation, the calculated value of D was 27.68 nm.

The FE-SEM image of the $Ni_{0.2}Zn_{0.2}Fe_{2.6}O_4$ in **Fig. 6A** indicates that the synthesized particles are almost spherical in shape and homogenous in distribution with a diameter less than 100 nm. **Fig. 6B** shows the distribution of the magnetic nanoparticles and P(PTA) on the surface of the CMC or embedding with the CMC that confirms the successful synthesis of the CMC/P(PTA)/$Ni_{0.2}Zn_{0.2}Fe_{2.6}O_4$ magnetic bionanocomposite.

Fig. 7 indicates the FT-IR spectrum for CMC, $Ni_{0.2}Zn_{0.2}Fe_{2.6}O_4$, P(PTA), and CMC/ P(PTA)/$Ni_{0.2}Zn_{0.2}Fe_{2.6}O_4$. The FT-IR spectrum of the $Ni_{0.2}Zn_{0.2}Fe_{2.6}O_4$ in **Fig. 7A** shows a broad band at 3424 cm^{-1}, and less intensive band at 1633 cm^{-1} related to the O-H groups stretching vibration [25]. The bands at 2925 and 2853 cm^{-1} are respectively assigned to the anti-symmetric and symmetric C-H vibrations of CTAB [26]. The band at 567 cm^{-1} attributes to the inherent metal stretching vibrations at the tetrahedral site (Fe-O), and the value of 478 cm^{-1} corresponds to the octahedral metal stretching (M-O) [25]. In **Fig. 7B**, the peaks related to the P(PTA) are as follows: 3164-3337 cm^{-1} (O-H and NH_2 stretching), 3054 cm^{-1} (C-H aromatic stretching), 2958 cm^{-1} (stretching of C-H aliphatic), 1683 cm^{-1} (stretching of C=O amide), 1641 cm^{-1} (stretching of

C=N), 1593 cm^{-1} (stretching of C=C), 1215 cm^{-1} (C-N), and 1167 cm^{-1} (C-O). The peaks in the FT-IR spectrum of CMC (**Fig. 7C**) shown at 3436, 1631, 1411, and 1061 cm^{-1} are respectively attributed to the stretching vibration of O-H, the carboxyl groups asymmetrical and symmetrical stretching, and stretching of C-O-C [27]. The comparison of the spectrum obtained for the CMC/P(PTA)/$Ni_{0.2}Zn_{0.2}Fe_{2.6}O_4$ (**Fig. 7D**) with other spectra expresses the successful synthesis of the bionanocomposite.

EDX was recorded to analyze the elements of the products, and the results are presented in **Fig. 8**. **Fig. 8A** shows Ni, Zn, Fe, and O peaks that confirm the formation of the $Ni_{0.2}Zn_{0.2}Fe_{2.6}O_4$. The elemental analysis of the nanocomposite in **Fig. 8B** represents similar peaks that are available in **Fig. 8A** along with the new peaks of N, S, and Ca due to the presence of the P(PTA) and CMC. Sodium peak is not seen in the spectrum of the CMC/P(PTA)/$Ni_{0.2}Zn_{0.2}Fe_{2.6}O_4$, suggesting that sodium ions were released completely from the matrix of sodium alginate into the solution during the crosslinking reaction process of sodium alginate with calcium.

The thermo-stability of the obtained P(PTA) and nanocomposite, analyzed using TGA/DTGA under N_2 atmosphere with the heating rate of 10 $^{\circ}$C/min, is presented in **Fig. 9**. As it is clear in **Fig. 9A**, there are five different weight-loss steps in the TGA curve of the P(PTA). Obviously, the first step (around 100 $^{\circ}$C) with a weight loss of 1.17 % can be attributed to water evaporation. The second step (from around 100 to 290 $^{\circ}$C) with the amount of 9.6 % weight loss can be attributed to the preliminary degradation of aliphatic groups of P(PTA). At the third step, ranging between 300 and 330 $^{\circ}$C, the aromatic groups of the P(PTA) are degrading gradually, and the forth step with the weight loss of 44.16 % corresponds to their further decomposition. The final step can be related to the complete degradation of the polymer residue and its

conversion to CO_2 and H_2O. **Fig. 9B** shows the TGA curve of the CMC/P(PTA)/$Ni_{0.2}Zn_{0.2}Fe_{2.6}O_4$. The thermal stability of the bionanocomposite compared to the pure P(PTA) has increased. It is obvious that the temperature of decomposition is shifted to higher temperatures due to the inorganic material existence in the matrix of the polymer, indicating that the thermal stability of the composite increases with the $Ni_{0.2}Zn_{0.2}Fe_{2.6}O_4$ loading.

According to the magnetic hysteresis loops in **Fig. 10A**, the $Ni_{0.2}Zn_{0.2}Fe_{2.6}O_4$ magnetic saturation value is about 45.87 emu/g that indicates superparamagnetic behavior of the synthesized product. Based on **Fig. 10B**, it is obvious that the synthesis process of the CMC/P(PTA)/$Ni_{0.2}Zn_{0.2}Fe_{2.6}O_4$ results in saturation magnetization reduction from 45.87 to 14.88 emu/g. This decrease is due to the combination of the magnetic nanoparticles with the P(PTA) and CMC. Despite this difference, the CMC/P(PTA)/$Ni_{0.2}Zn_{0.2}Fe_{2.6}O_4$ could be easily separated from aqueous solution by an external magnetic field to avoid secondary pollution. As indicated in **Fig. 10C**, the metal ions-loaded adsorbent is separated easily by applying an external magnetic field from the solution due to its high magnetization value.

3.2. pH effect

The influence of initial solution pH is considered as a major factor to obtain high adsorption efficiency during adsorption process. To analyze the influence of the pH of the solution on the adsorption efficiency of Nd^{+3}, Tb^{+3}, and Dy^{+3} by the CMC/P(PTA)/$Ni_{0.2}Zn_{0.2}Fe_{2.6}O_4$, the pH value was considered between 1.5 and 5.5. As it is clear in **Fig. 11A**, the adsorption of the metal ions is significantly associated with the value of pH since it influences the metal ions solubility and the ionization status of the groups available on the CMC/P(PTA)/$Ni_{0.2}Zn_{0.2}Fe_{2.6}O_4$. The obtained results state that the metal ions adsorption efficiency on the adsorbent surface increases remarkably with pH value increase from 1.5 to 5.5 because the interaction between hydrogen and

metal cations for binding the active sites reduces. The little protonation of the functional groups also inhibits the relation between the adsorbent and the metal ions that could be the major cause for a low value of adsorption efficiency at lower pH values [28]. The influence of solution pH on the metal ions adsorption was not studied for a pH > 5.5 in order to prevent the metal ions precipitation formation as the hydroxides. Therefore, solution pH = 5.5 was applied as an optimum value for further adsorption studies.

3.3. Contact time effect

One of the key factors in treatment of a sample is the contact time of solution and adsorbent as it can present the interaction kinetics of an adsorbent with an adsorbate. Therefore, the influence of contact time on Nd^{+3}, Tb^{+3}, and Dy^{+3} ions adsorption onto the CMC/P(PTA)/$Ni_{0.2}Zn_{0.2}Fe_{2.6}O_4$ was studied at 25 $^{\circ}$C and 30 mg/L of each metal ion. The obtained results in **Fig. 11B** indicate that the quantities of Nd^{+3}, Tb^{+3}, and Dy^{+3} adsorbed per unit mass of the adsorbent increase by an enhancement in contact time, and adsorption efficiencies of 60.07, 63.56, and 63.96 % are respectively obtained for Nd^{+3}, Tb^{+3}, and Dy^{+3} within 50 min. The plots in **Fig. 11B** indicate two phases for the metal ions adsorption. The sharper portion at the first phase is related to a great number of empty active sites on the surface of the adsorbent and high concentration of the ions. The second step is assigned to the decrease in IPD with contact time that leads to an equilibrium state. The reason for this condition is the external active sites saturation and low ions concentration [29]. As can be seen, the required time to achieve an equilibrium state is 90 min for all ions, and a further increase in contact time does not have any significant influence on the metal ions adsorption. Therefore, further experiments were performed by considering the optimum contact time of 90 min.

3.4. Kinetics of adsorption

The parameters of adsorption kinetics are extremely useful in the application of adsorbents since they control adsorbate uptake residence time at the interface of solid and solution and can augment the realization of designing a water treatment process. Kinetic data analysis provides significant data about the mechanism of adsorption that is helpful for designing and modeling the process of adsorption. Hence, three different kinetic models as pseudo-first order (PFO), PSO, and IPD models were employed to fit the experimental data. The non-linear regression forms of the models were applied as follows [30,31]:

$q_t = q_e\,(1 - \exp^{-K_1 t})$ (PFO) (5)

$q_t = K_2 q_e^2 t/1 + K_2 q_e t$ (PSO) (6)

$q_t = K_i t^{0.5} + C$ (IPD) (7)

Where K_1 (1/min) and K_2 (g/mg min) respectively refer to PFO rate constant and PSO rate constant, and K_i (1/min) shows the rate constant of IPD. Moreover, C provides data about the thickness of the boundary layer. Notably, the greater value of C is related to the influence of the boundary layer diffusion.

The initial rate of adsorption (h) can be obtained using K_2 and q_e values via the following equation:

$h = K_2 q_e^2$ (8)

Non-linear regression analysis of the empirical data can be used to acquire the kinetic models constant values. The obtained kinetic parameters are presented in **Table 1**. The coefficient of determination (R^2) and Chi-square (χ^2) was also employed to evaluate the conformity between the experimental data and the computed values. χ^2 is defined as follows:

$$\chi^2 = \sum_{i=1}^{n} \frac{(q_{e,exp} - q_{e,cal})^2}{q_{e,cal}} \quad (9)$$

Where $q_{e,exp}$ and $q_{e,cal}$ respectively refer to the experimental and computed adsorbent capacities, and n shows data point numbers.

The kinetic parameters in **Table 1** show that the R^2 values of 0.9629, 0.9564, and 0.9686 respectively acquired by PSO model for Nd^{+3}, Tb^{+3}, and Dy^{+3} are greater than those of PFO model (0.8831, 0.8538, and 0.8803). The values of χ^2 are also lower than those of PFO model. The values of q_e computed by PSO model are in agreement with the values of the experimental q_e, implying the chemisorption of the process. The R^2 and χ^2 values obtained by fitting IPD model to the empirical data show that it is also appropriate for explaining the adsorption kinetic of Nd^{+3}, Tb^{+3}, and Dy^{+3} onto the CMC/P(PTA)/$Ni_{0.2}Zn_{0.2}Fe_{2.6}O_4$. Thus, it can be mentioned that Nd^{+3}, Tb^{+3}, and Dy^{+3} adsorption processes follow both IPD and PSO kinetic models.

3.5. Adsorbent dosage effect

Nd^{+3}, Tb^{+3}, and Dy^{+3} ions adsorption onto the CMC/P(PTA)/$Ni_{0.2}Zn_{0.2}Fe_{2.6}O_4$ was studied using 30 mg/L initial ions concentration at pH = 5.5 within 90 min. As can be seen in **Fig. 11C**, by an enhancement in adsorbent dosage in the range of 0.01 to 0.07 g, adsorption efficiency increases. The reason is that the metal ions compete for confined adsorption sites at lower adsorbent dosage. However, by increasing the adsorbent dosage, a greater surface area and more empty sites are available; therefore, adsorption efficiency increases [32]. The maximum adsorption efficiency is 98.15 % for Nd^{+3}, 97.6 % for Tb^{+3}, and 99.42 % for Dy^{+3} using 0.06 g of the adsorbent. The adsorption efficiency of the ions smoothly increases with the adsorbent up to 0.07 g. Consequently, 0.06 g of the adsorbent was considered as an optimum dosage for further experiments.

3.6. Initial concentration effect

The initial adsorbate concentration is considered as an essential driving force to overcome the adsorbate mass transfer resistance between the solid and aqueous phases. The initial concentration influence of Nd^{+3}, Tb^{+3}, and Dy^{+3} on the adsorption efficiency is presented in **Fig. 11D**. The adsorption efficiency respectively decreases from 98.15 to 16.74, 97.6 to 21.4 5, and 99.42 to 21.76 % for Nd^{+3}, Tb^{+3}, and Dy^{+3}. By calculating the amount of q_e, it was seen that by enhancing initial concentration from 30 to 300 mg/L, q_e increased from 24.52 to 41.88, 24.76 to 53.62, and 24.87 to 54.33 mg/g for Nd^{+3}, Tb^{+3}, and Dy^{+3}, respectively. These results show that Nd^{+3}, Tb^{+3}, and Dy^{+3} adsorption is dependent on the concentration of the metal ions since it supplies the major driving force for overcoming limitations of mass transfer between the solid and the aqueous phases. The adsorption is not influenced by the initial ion concentration when the concentration of the ion is low that is owing to the great number of binding sites while being easily accessible for adsorption. The value of adsorption efficiency decreases at higher ion concentration for a constant content of adsorbent because the quantity of the accessible sites of adsorption on the surface of the adsorbent decreases and therefore their saturation takes place easily. As a result, by occupying valence forces via exchanging or sharing electron and complexation, more mass transfer from the liquid stage occurs, which is fairly known as a slow process [33].

3.7. Adsorption isotherms

For the optimization of adsorbent usage in an adsorption process, knowing that how solutes interact with adsorbent is so important. In this case, adsorption isotherms can explain the interaction between adsorbate quantity adsorbed onto adsorbent and dissolved adsorbate concentration at equilibrium state. In this paper, Freundlich and Langmuir isotherm models were applied for fitting the obtained data at equilibrium and evaluating the adsorption properties of

Nd^{+3}, Tb^{+3}, and Dy^{+3} onto the CMC/P(PTA)/$Ni_{0.2}Zn_{0.2}Fe_{2.6}O_4$. The nonlinear forms of Langmuir and Freundlich are respectively defined by Eqs. (10) and (11) [34,35].

$$q_e = \frac{b\ q_m\ C_e}{(1+bC_e)} \quad (10)$$

$$q_e = K\ C_e^{1/n} \quad (11)$$

The isotherm parameters including q_m (the maximum capacity at saturation state (mg/g)), b (constant of Langmuir (L/mg)), K (capacity of adsorption ($mg^{1-1/n}\ L^{1/n}/g$)), and 1/n (adsorption intensity) are shown in **Table 2**. The means of the dimensionless factor ($R_L=\frac{1}{1+bC_i}$) can be used to appraise the desirability of the adsorption process in the Langmuir model as following: irreversible ($R_L = 0$), favorable ($0 < R_L < 1$), linear ($R_L = 1$), and unfavorable ($R_L > 1$) adsorption [36]. According to the Langmuir adsorption constants (**Table 2**), the R_L values of 0.001, 0.0022, and 0.0005 respectively acquired for Nd^{+3}, Tb^{+3}, and Dy^{+3} are between 0 and 1 that show the adsorption of the ions onto the adsorbent is favorable. In addition, the results of the adsorption isotherms presented in **Table 2** indicate that the 1/n values of 0.09, 0.13, and 0.12 for Nd^{+3}, Tb^{+3}, and Dy^{+3}, respectively, obtained from Freundlich model are representative of highly curved isotherms due to the values of $1/n < 0.7$. The results show that the experimental data for Nd^{+3}, Tb^{+3}, and Dy^{+3} adsorption onto the CMC/P(PTA)/$Ni_{0.2}Zn_{0.2}Fe_{2.6}O_4$ are fitted with Freundlich isotherm model with R^2 values of 0.9709, 0.9482, and 0.9632, respectively, that are higher than those acquired by Langmuir isotherm model. The lower values of χ^2 also confirm the obtained results for each ion. In the present study, the results of fitting experimental data show that the adsorption of the metal ions is performed by the sites of the adsorbent that are heterogeneous, indicating non-uniform and multi-layer adsorption. A comparison of the adsorption capacity of different adsorbents is represented in **Table 3**.

3.8. Ionic strength effect

The existence of salts as the most available materials in real samples as an interfering agent can affect the adsorption efficiency of the target ion that leads to strengthen or weaken its adsorption. Thus, in the present study, the $NaNO_3$ solutions with various concentrations (0.02, 0.04, 0.06, 0.08, and 0.1 M) were utilized to evaluate the ionic strength influence on Nd^{+3}, Tb^{+3}, and Dy^{+3} ions adsorption onto the CMC/P(PTA)/$Ni_{0.2}Zn_{0.2}Fe_{2.6}O_4$ under the optimum conditions. The results in **Fig. 12A** indicate a reduction in the adsorption efficiency with an enhancement in the concentration of $NaNO_3$ from 0.02 to 0.1 M that may be explained by the occurrence of competition between the Na^+ cations from the salt and cationic ions for the occupation of the adsorbent active sites. The adsorption efficiency of Dy^{+3} decreases from 96.6 to 94.1 % that is lower than those obtained for Nd^{+3} and Tb^{+3}, indicating that the concentration of $NaNO_3$ has higher negative effect on the adsorption of Nd^{+3} and Tb^{+3}, specifically Nd^{+3}.

3.9. Temperature effect and evaluation of thermodynamic parameters

The parameters of thermodynamic (ΔH^o (kJ/mol), ΔS^o (kJ/mol K), and ΔG^o (kJ/mol)) were evaluated at 25, 35, and 45 $^{\circ}$C to consider the effect of temperature on the performance of adsorption and find the adsorption mechanism by the following equations [61]:

$$K_d = q_e/C_e \quad (12)$$

$$\text{Ln } K_d = \Delta S^{\circ}/R - \Delta H^{\circ}/RT \quad (13)$$

$$\Delta G^{\circ} = - RT \text{ Ln } K_d \quad (14)$$

Where R (8.314 J/mol K) shows the gas constant, T shows the temperature (K), and K_d refers to the distribution coefficient. C_e shows the equilibrium concentration of ion in the solution (mg/L). As can be seen in **Table 4**, adsorption efficiency increases for all metal ions by an increase in temperature. ΔH^o and ΔS^o values in Eq. (13) were respectively acquired from the slope and intercept of the Ln K_d versus 1/T plot (**Fig. 12B**). The thermodynamic parameters are presented

in **Table 4**. K_d value increases by enhancing the temperature that indicates the process is endothermic in nature. The values of ΔG^o are low that indicate the strong adsorptive forces, spontaneous adsorption process, and better adsorption at a higher temperature. The adsorption of the ions is not spontaneous at low temperature. $\Delta H^o > 0$ reveals that the ions adsorption is endothermic, and their adsorption efficiency increases with increasing temperature. $\Delta S^o > 0$ demonstrates that there is a good affinity between the ions and the adsorbent, and randomness increases at the interface of the solid-solution during the process. In conclusion, the thermodynamic parameters reveal endothermic adsorption process, an affinity of the adsorbent for the ions, and spontaneous nature of Nd^{+3}, Tb^{+3}, and Dy^{+3} adsorption onto the adsorbent by rising temperature.

3.10. Reusability studies

One of the main parameters in the adsorption process is adsorbent reusability as it makes the process economically feasible. To evaluate the reusability of the CMC/P(PTA)/$Ni_{0.2}Zn_{0.2}Fe_{2.6}O_4$, 50 mL of 0.2 M HNO_3 was applied as the eluent. First, metal ions adsorption was done by the addition of 0.06 g of the adsorbent into 50 mL solution of 30 mg/L of metal ions at optimum conditions. The adsorbent loaded with the ions was separated by an external magnetic field, washed several times with DW and finally dried at 40 ˚C. Then, the desorption process was performed by using the eluent for 2 h. After the desorption process, the metal ions in the solutions were measured, and the adsorbent was neutralized and further used for the ions adsorption in the cycles. Nd^{+3}, Tb^{+3}, and Dy^{+3} ions were desorbed from the adsorbent > 82, 84, and 88 %, respectively. Four cycles of adsorption-desorption were performed to evaluate the reuse efficiency of the adsorbent. The results in **Fig. 12C** show that the CMC/P(PTA)/$Ni_{0.2}Zn_{0.2}Fe_{2.6}O_4$ adsorption efficiency respectively decreases from 97.29 to 86.43,

96.47 to 84.61, and 98.54 to 87.52 % for Nd^{+3}, Tb^{+3}, and Dy^{+3} after the fourth cycle that indicates metal ions may chemically bond with the groups on the adsorbent surface.

3.11. Competitive adsorption

To evaluate competitive adsorption of Nd^{+3}, Tb^{+3}, and Dy^{+3} in the ternary system of 30 mg/L (1:1:1), 0.06 g of the CMC/P(PTA)/$Ni_{0.2}Zn_{0.2}Fe_{2.6}O_4$ (the same as a single system) was used. According to the value of q_{mix}/q_0, three kinds of influences can occur in a multicomponent system as following:

- Antagonism ($q_{mix}/q_0 < 1$): effect of mixture of component in solution is less than its individual effect.
- Synergism ($q_{mix}/q_0 > 1$): effect of mixture of component in solution is greater than its individual effect.
- Non-interaction ($q_{mix}/q_0 = 1$): effect of mixture of component in solution is neither less nor more than that of its individual effect.

Where q_{mix} and q_0 are respectively the adsorption capacities of each ion in the mixture and single systems.

The value of q_{mix}/q_0 was respectively obtained to be 0.2, 0.38, and 0.41 for Nd^{+3}, Tb^{+3}, and Dy^{+3}. The obtained results indicate that the q_{mix}/q_0 value for all ions is < 1 in the ternary mixture; therefore, the existence of each ion shows an antagonism effect on the other ions adsorption. The adsorption efficiency for Nd^{+3}, Tb^{+3}, and Dy^{+3} respectively decreased to 19.4, 37.6, and 40.9 %. EDX spectrum was also recorded after the adsorption process, and the result is presented in **Fig. 12D**. The existence of Nd^{+3}, Tb^{+3}, and Dy^{+3} peaks in the spectrum strongly confirms the successful adsorption of the ions by the CMC/P(PTA)/$Ni_{0.2}Zn_{0.2}Fe_{2.6}O_4$.

4. Conclusion

In this research, the novel biodegradable nanoporous P(PTA) was synthesized by polycondensation reaction of TMAPD in {[1,3-(pr)2im]Br} ionic liquid as green media. Then, the CMC/$Ni_{0.2}Zn_{0.2}Fe_{2.6}O_4$ magnetic bionanomposite containing the P(PTA) was fabricated. The successful synthesis of the products was approved by FE-SEM, EDX, NMR, XRD, FT-IR, and VSM techniques. The prepared bionanocomposite showed favorable magnetization value of 14.88 emu/g that was enough to be easily separated by a magnetic field from aqueous medium. Then, it was used to investigate the adsorption of Nd^{+3}, Tb^{+3}, and Dy^{+3}. For obtaining the maximum adsorption efficiency of the ions at the concentration of 30 mg/L, the optimum conditions were obtained at pH = 5.5, the adsorbent dosage of 0.06 g, and contact time of 90 min. The adsorption efficiency values of 98.15, 97.6, and 99.42 % were respectively obtained for Nd^{+3}, Tb^{+3}, and Dy^{+3} at optimum conditions. The adsorption kinetics followed PSO and IPD models, and Freunlich model was suitable for fitting the adsorption data of the metal ions obtained at equilibrium. The adsorption efficiency for the ions greatly decreased in the presence of $NaNO_3$ as ionic strength. The thermodynamic parameters revealed that the spontaneous nature of Nd^{+3}, Tb^{+3}, and Dy^{+3} adsorption onto the adsorbent can be occurred by increasing temperature. The competitive adsorption of the ions showed that the existence of each ion had antagonism effect on the other ions adsorption. The results show that the CMC/P(PTA)/$Ni_{0.2}Zn_{0.2}Fe_{2.6}O_4$ is an efficient and potential adsorbent with a favorable performance for practical applications in Nd^{+3}, Tb^{+3}, and Dy^{+3} ions adsorption process.

Acknowledgments

This work has been supported by the Spanish Ministry of Economy and Competitiveness (Ref. CTM2017-83581-R). Hamedreza Javadian acknowledges the financial support received (Ref. BES-2015-072506).

References

[1] I. Liatsou, M. Efstathiou, I. Pashalidis, Adsorption of trivalent lanthanides by marine sediments. J. Radioanal. Nucl. Chem. 304 (2015) 41–45.

[2] I. Anastopoulos, A. Bhatnagar, E.C. Lima, Adsorption of rare earth metals: A review of recent literature. J. Mol. Liq. 221 (2016) 954–962.

[3] J. Jacinto, B. Henriques, A.C. Duarte, C. Vale, E. Pereira, Removal and recovery of critical rare earth elements from contaminated waters by living *Gracilaria gracilis*. J. Hazard. Mater. 344 (2018) 531–538.

[4] J. Ponou, L.P. Wang, G. Dodbiba, K. Okaya, T. Fujita, K. Mitsuhashi, T. Atarashi, G. Satoh, M. Noda, Recovery of rare earth elements from aqueous solution obtained from vietnamese clay minerals using dried and carbonized parachlorella. J. Environ. Chem. Eng. 2 (2014) 1070–1081.

[5] Y.R. Smith, D. Bhattacharyya, T. Willhard, M. Misra, Adsorption of aqueous rare earth elements using carbon black derived from recycled tires. Chem. Eng. J. 296 2016 102–111.

[6] V.N. Rychkov, E.V. Kirillov, S.V. Kirillov, V.S. Semenishchev, G. M. Bunkov, M.S. Botalov, D.V. Smyshlyaev, A.S. Malyshev, Recovery of rare earth elements from phosphogypsum. J. Clean. Prod. 196 (2018) 674–681.

[7] V. Fernandez, Rare-earth elements market: A historical and financial perspective, Resour. Policy 53 (2017) 26–45.

[8] M. Alemrajabi, A.C. Rasmuson, K. Korkmaz, K. Forsberg, Recovery of rare earth elements from nitrophosphoric acid solutions. Hydrometallurgy 169 (2017) 253–262.

[9] A. Battsengel, A. Batnasan, A. Narankhuu, K. Haga, Y. Watanabe, A. Shibayama, Recovery of light and heavy rare earth elements from apatite ore using sulphuric acid leaching, solvent extraction and precipitation. Hydrometallurgy 179 (2018) 100–109.

[10] L. Jiang, W. Zhang, C. Luo, D. Cheng, J. Zhu, Adsorption toward trivalent rare earth element from aqueous solution by zeolitic imidazolate frameworks, Ind. Eng. Chem. Res. 55 (2016) 6365-6372.

[11] Z.V.P. Murthy, A. Choudhary, Separation and estimation of nanofiltration membrane transport parameters for cerium and neodymium. Rare Met. 31 (2012) 500−506.

[12] L. Fan, C. Luo, Z. Lv, F. Lu, H. Qiu, Removal of Ag^{+} from water environment using a novel magnetic thiourea-chitosan imprinted Ag^{+}, Journal of Hazardous Materials 194(11) (2011) 193-201.

[13] G. Cravotto, S. Tagliapietra, B. Robaldo, M. Trotta, Chemical modification of chitosan under high-intensity ultrasound, Ultrason. Sonochem. 12 (2005)95–98.

[14] K. Kurita, Controlled functionalization of the polysaccharide chitin, Prog. Polym. Sci. 26 (2001) 1921–1971.

[15] N.K. Patel, V.K. Sinha, Synthesis, characterization and optimization of water-soluble chitosan derivatives, Int. J. Polym. Mater. Polym. Biomater. 58 (2009) 548-560.

[16] S. Zhao, F. Zhou, L. Li, M. Cao, D. Zuo, H. Liu, Removal of anionic dyes from aqueous solutions by adsorption of chitosan-based semi-IPN hydrogel composites, Compos. Part B: Eng. 43 (2012) 1570–1578.

[17] D.W. Cho, B.H. Jeon, C.M. Chon, Y. Kim, F.W. Schwartz, E.S. Lee, H. Song, A novel chitosan/clay/magnetite composite for adsorption of Cu(II) and As(V), Chem. Eng. J. 200-202(34) (2012) 654-662.

[18] J. Lu, F. Yan, J. Texter, Advanced applications of ionic liquids in polymer science, Prog. Polym. Sci. 34 (2009) 431-448.

[19] M. Taghavi, M. Ghaemy, S.M. AminiNasab, M. Hassanzadeh, Influence of ionic liquid on selective polycondensation of a new diamine-bisphenol: Synthesis and properties of polyamides and their composites with modified nanosilica, Polymer 54 (2013) 3828-3840.

[20] A.M. Bochek, N.M. Zabivalova, E.N. Brazhnikova, M.S. Anferova, V.K. Lavrent'ev, Chitosan—polyamide composite nanofibers produced by needleless electrospinning, Fibre Chem 50 (2019) 391–395.

[21] D.L. Francisco, L.B. Paiva, W. Aldeia, Advances in polyamide nanocomposites: A review, Polym. Composite. 40 (2019) 851-870.

[22] Y.S. Vygodskii, E.I. Lozinskaya, A.S. Shaplov, K.A. Lyssenko, M.Y. Antipin, Y.G. Urman, Implementation of ionic liquids as activating media for polycondensation processes, Polymer 45 (2004) 5031–5045.

[23] D. Ni, Z. Lin, P. Xiaoling, W. Xinqing, G. Hongliang, Preparation and characterization of nickel-zinc ferrites by a solvothermal method, Rare. Metal. Mat. Eng. 44(9) (2015) 2126-2131.

[24] R. Rahmawati, M. Gilang Permana, B. Harison, Nugraha, B. Yuliarto, Suyatman, D. Kurniadi, Optimization of frequency and stirring rate for synthesis of magnetite (Fe_3O_4) nanoparticles by using coprecipitation-ultrasonic irradiation methods, Procedia Eng. 170 (2017) 55–59.

[25] A.S.A. Bakr, Y.M. Moustafa, E.A. Motawea, M.M. Yehia, M.M.H. Khalil, Removal of ferrous ions from their aqueous solutions onto $NiFe_2O_4$–alginate composite beads, J. Environ. Chem. Eng. 3 (2015) 1486–1496.

[26] S.A. Elfeky, S. Ebrahim Mahmoud, A. Fahmy Youssef, Applications of CTAB modified magnetic nanoparticles for removal of chromium (VI) from contaminated water, J Adv Res. 8(4) (2017) 435–443.

[27] V. Gopalakannan, N. Viswanathan, Synthesis of magnetic alginate hybrid beads for efficient chromium(VI) removal, Int. J. Biol. Macromol. 72 (2015) 862–867.

[28] P. Kampalanonwat, P. Supaphol, The study of competitive adsorption of heavy metal ions from aqueous solution by aminated polyacrylonitrile nanofiber mats, Energy Procedia 56 (2014) 142–151.

[29] A. Afkhami, M. Saber-Tehrani, H. Bagheri, Simultaneous removal of heavy-metal ions in wastewater samples using nano-alumina modified with 2,4-dinitrophenylhydrazine, J. Hazard. Mater. 181 (2010) 836–844.

[30] H. Javadian, B. Babzadeh Koutenaei, E. Shekarian, F. Zamani Sorkhrodi, R. Khatti, M. Toosi, Application of functionalized nano HMS type mesoporous silica with N-(2-aminoethyl)-3-aminopropyl methyldimethoxysilane as a suitable adsorbent for removal of Pb (II) from aqueous media and industrial wastewater, J. Saudi. Chem. Soc. 21 (2017) S219-S230.

[31] H. Javadian, M. Torabi Angaji, M. Naushad, Synthesis and characterization of polyaniline/γ-alumina nanocomposite: A comparative study for the adsorption of three different anionic dyes, J. Ind. Eng. Chem. 20 (2014) 3890-3900.

[32] T.T.N. Le, V.T. Le, M.U. Dao, Q.V. Nguyen, T.T. Vu, M.H. Nguyen, D.L. Tran, H.S. Le, Preparation of magnetic graphene oxide/chitosan composite beads for effective removal of heavy metals and dyes from aqueous solutions, Chem. Eng. Commun. 206 (2019) 1337-1352.

[33] K.M. Seema, B.B. Mamba, J. Njuguna, R.Z. Bakhtizin, A.K. Mishra, Removal of lead (II) from aqueous waste using (CD-PCL-TiO_2) bio-nanocomposites, Int. J. Biol. Macromol. 109 (2018) 136-142.

[34] H. Javadian, Adsorption performance of suitable nanostructured novel composite adsorbent of poly(N-methylaniline) for removal of heavy metal from aqueous solutions, J. Ind. Eng. Chem. 20 (2014) 4344-4352.

[35] H. Javadian, Application of kinetic, isotherm and thermodynamic models for the adsorption of Co(II) ions on polyaniline/polypyrrole copolymer nanofibers from aqueous solution, J. Ind. Eng. Chem. 20 (2014) 4233-4241.

[36] S. Liu, B. Huang, L. Chai, Y. Liu, G. Zeng, X. Wang, W. Zeng, M. Shang, J. Deng, Z. Zhou, Enhancement of As(V) adsorption from aqueous solution by a magnetic chitosan/biochar composite, RSC Adv. 7 (2017) 10891–10900.

[37] E. Liu, X. Zheng, X. Xu, F. Zhang, E. Liu, Y. Wang, C. Li, Y. Yan, Preparation of diethylenetriamine-modified magnetic chitosan nanoparticles for adsorption of rare-earth metal ions, New J. Chem. 41 (2017) 7739-7750.

[38] J. Roosen, K. Binnemans, Adsorption and chromatographic separation of rare earths with EDTA- and DTPAfunctionalized chitosan biopolymers. J Mater Chem A. 2 (2014) 1530–1540.

[39] I.V. Melnyk, V.P. Goncharyk, L.I. Kozhara, G.R. Yurchenko, A.K. Matkovsky, Y.L. Zub, B. Alonso, Sorption properties of porous spray-dried microspheres functionalized by phosphonic acid groups, Microporous Mesoporous Mater. 153 (2012) 171–177.

[40] T. Kegl, I. Ban, A. Lobnik, A. Košak, Synthesis and characterization of novel γ-Fe_2O_3-NH_4OH@SiO_2(APTMS) nanoparticles for dysprosium adsorption, J. Hazard. Mater. 378 (2019) 120764.

[41] S. Iftekhar, V. Srivastava, A. Casas, M. Sillanpää, Synthesis of novel GA-g-PAM/SiO_2 nanocomposite for the recovery of rare earth elements (REE) ions from aqueous solution. J Clean Prod. 170 (2018) 251-259.

[42] S. Iftekhar, V. Srivastava, S. Ben Hammouda, M. Sillanpää, Fabrication of novel metal ion imprinted xanthan gum-layered double hydroxide nanocomposite for adsorption of rare earth elements, Carbohydr Polym. 194 (2018) 274–284.

[43] T. Ogata, H. Narita, M. Tanaka, Rapid and selective recovery of heavy rare earths by using an adsorbent with diglycol amic acid group, Hydrometallurgy. 155 (2015) 105-109.

[44] S.M.A. Koochaki-Mohammadpour, M. Torab-Mostaedi, A. Talebizadeh-Rafsanjani, F. Naderi-Behdani, Adsorption isotherm, kinetic, thermodynamic, and desorption studies of lanthanum and dysprosium on oxidized multiwalled carbon nanotubes. J Dispers Sci Technol 35 (2014) 244–254.

[45] Y.R. Smith, D. Bhattacharyya, T. Willhard, M. Misra, Adsorption of aqueous rare earth elements using carbon black derived from recycled tires, Chem Eng J 296 (2016) 102–111.

[46] X. Xu, X-Y. Jiang, F-P. Jiao, X-Q. Chen, J-G. Yu, Tunable assembly of porous three-dimensional graphene oxide-corn zein composites with strong mechanical properties for adsorption of rare earth elements, J Taiwan Inst Chem Eng 85 (2018) 106-114.

[47] H.A. Madbouly, N.E. El-Hefny, Y.A. El-Nadi, Adsorption and separation of terbium(III) and gadolinium(III) from aqueous nitrate medium using solid extractant, Sep Sci Technol. (2019) 1-13.

[48] S. Tong, S. Zhao, W. Zhou, R. Li, Q. Jia, Modification of multi-walled carbon nanotubes with tannic acid for the adsorption of La, Tb and Lu ions, Microchim Acta 174 (2011) 257–264.

[49] D. Baybaş, U. Ulusoy, Polyacrylamide–clinoptilolite/Y-zeolite composites: Characterization and adsorptive features for terbium, J Hazard Mater 187(1) (2011) 241–249.

[50] R. Akkaya, Synthesis and characterization of a new low-cost composite for the adsorption of rare earth ions from aqueous solutions, Chem Eng J 200 (2012) 186–191.

[51] R. Akkaya, Terbium adsorption onto polyhydroxyethylmethacrylate–hydroxyapatite composite and its modified composition by phytic acid, Desalin Water Treat 52 (2014) 1440-1447.

[52] Ó. Barros, L. Costa, F. Costa , A. Lago, V. Rocha, Z. Vipotnik, B. Silva, T. Tavares, Recovery of rare earth elements from wastewater towards a circular economy, Molecules 24 (2019) 1005.

[53] N.S. Reddy, K.M. Rao, S.V. Krishna, C.S. Ha, Synthesis of 1–acryloyl–3–phenyl thiourea based pH sensitive hydrogels for removal of samarium and terbium, Macromol. Res. 24 (2016) 494–501.

[54] M.R. Awual, N.H. Alharthi, Y. Okamoto, M.R. Karim, M.E. Halim, M.M. Hasan, M.M. Rahman, M.M. Islam, M.A. Khaleque, M.C. Sheikh, Ligand field effect for Dysprosium(III) and Lutetium(III) adsorption and EXAFS coordination with novel composite nanomaterials, Chem. Eng. J. 320 (2017) 427-435.

[55] Y.R. Lee, K. Yu, S. Ravi, W.S. Ahn, Selective adsorption of rare earth elements over functionalized Cr-MIL-101. Appl Mater Interfaces. 10 (2018) 23918-23927.

[56] R.M. Ashour, R. El-Sayed, A.F. Abdel-Magied, A.A. Abdel-Khalek, M.M. Ali, K. Forsberg, A. Uheida, M. Muhammed, J. Dutta, Selective separation of rare earth ions from aqueous solution using functionalized magnetite nanoparticles: kinetic and thermodynamic studies, Chem. Eng. J. 327 (2017) 286–296.

[57] H. Aghayan, A. Mahjoub, A. Khanchi, Samarium and dysprosium removal using 11-molybdo-vanadophosphoric acid supported on Zr modified mesoporous silica SBA-15, Chem. Eng. J. 225 (2013) 509–519.

[58] T. Kaneko, F. Nagata, S. Kugimiya, K. Kato, Optimization of carboxyl-functionalized mesoporous silica for the selective adsorption of dysprosium, J. Environ. Chem. Eng. 6 (2018) 5990-5998.

[59] X. Zheng, Y. Zhang, T. Bian, Y. Zhang, Z. Li, J. Pan, Oxidized carbon materials cooperative construct ionic imprinted cellulose nanocrystals films for efficient adsorption of Dy(III), Chem Eng J 381 (2020) 122669.

[60] X. Zheng, E. Liu, F. Zhang, Y. Yan, J. Pan, Efficient adsorption and separation of dysprosium from NdFeB magnets in an acidic system by ion imprinted mesoporous silica sealed in a dialysis bag, Green Chem. 18 (2016) 5031–5040.

[61] K. Zhu, Y. Duan, F. Wang, P. Gao, H. Jia, C. Ma, C. Wang, Silane-modified halloysite/Fe_3O_4 nanocomposites: Simultaneous removal of Cr(VI) and Sb(V) and positive effects of Cr(VI) on Sb(V) adsorption, Chem. Eng. J. 311 (2017) 236-246.

Table 1. Kinetic constants for adsorption of the ions by the CMC/P(PTA)/$Ni_{0.2}Zn_{0.2}Fe_{2.6}O_4$.

		Nd^{+3}	Tb^{+3}	Dy^{+3}
PFO	K_1 (1/min)	0.116	0.132	0.126
	q_e (mg/g)	31.15	32.29	32.71
	R^2	0.8831	0.8538	0.8803
	χ^2	7.24	8.77	7.52
PSO	K_2 (g/mg min)	0.0043	0.0049	0.0047
	q_e (mg/g)	34.85	35.80	36.27
	h (mg/g min)	5.22	6.28	6.18
	R^2	0.9629	0.9564	0.9686
	χ^2	2.3	2.61	1.97
IPD	K_i (1/min)	11.16	11.02	11.20
	R^2	0.9737	0.9782	0.9676
	χ^2	1.63	1.31	2.03

Table 2. Isotherm constants for adsorption of the ions by the CMC/P(PTA)/$Ni_{0.2}Zn_{0.2}Fe_{2.6}O_4$.

		Nd^{+3}	Tb^{+3}	Dy^{+3}
Langmuir	b (L/mg)	3.28	1.51	6.391
	q_m (mg/g)	36.59	42.87	43.76
	R_L	0.001	0.0022	0.0005
	R^2	0.5679	0.5398	0.5771
	χ^2	16.7	43.21	47.31
Freundlich	K ($mg^{1-1/n}$ $L^{1/n}$/g)	24.23	23.7	26.13
	1/n	0.09	0.13	0.12
	R^2	0.9709	0.9482	0.9632
	χ^2	1.12	4.86	4.12

Table 3. Comparison of the adsorption capacity of Nd^{+3}, Tb^{+3}, and Dy^{+3} onto various adsorbents.

Adsorbent	q_m (mg/g)			Reference
	Nd^{+3}	Tb^{+3}	Dy^{+3}	
Fe_3O_4-C_{18}-chitosan-DETA	27.1		28.3	[37]

EDTA functionalized chitosan	74			[38]
Phosphonic acid functionalized silica microspheres	45			[39]
γ-Fe_2O_3-NH_4OH@SiO_2(APTMS)		46.5	23.2	[40]
GA-g-PAM/SiO_2	12.24			[41]
Zr@XG-ZA	14.01[a]			[42]
EDASiDGA	16.15			[43]
Oxidized multi-walled carbon nanotubes			78.12	[44]
Carbon black derived from recycled tires	0.67			[45]
3D GO-CZ	9.68			[46]
Macroporous polymeric resin (TVEX-PHOR)		24.93		[47]
TA-MWCNTs		8.55		[48]
YZ		44.5		[49]
Poly(acrylamide-expanded perlite) [P(AAm-EP)]		118.3		[50]
P(HEMA-Hap)-phy		49.27		[51]
Supported biomass on zeolite (SBZ)		5.07		[52]
Acryloyl–phenyl thiourea		74.23		[53]
Hybrid Lewis base ligands functionalized alumina-silica			125.4	[54]
MIL-101-PMIDA	70.9			[55]
CA@Fe_3O_4 NPs	41			[56]
11-Molybdo-vanadophosphoric acid supported on Zr modified mesoporous silica SBA-15			50	[57]

MPS (22 nm)-2NH-2COOH			44.8	[58]
o-CNCs-IIPs			28.97	[59]
o-CNCs/o-MWCNTs-IIPs			38.7	[59]
o-CNCs/GO-IIPs			41.79	[59]
Imprinted mesoporous silica materials			22.33	[60]
CMC/P(PTA)/$Ni_{0.2}Zn_{0.2}Fe_{2.6}O_4$	39.82[a]	50.32[a]	48.23[a]	This study

[a] Calculated from Freundlich isotherm

Table 4. Effect of temperature on the adsorption of the ions at 90 mg/L and thermodynamic parameters.

		Adsorption efficiency (%)		
Temperature (°C)		Nd^{+3}	Tb^{+3}	Dy^{+3}
25		45.72	50.58	52.61
35		51.05	57.51	59.89
45		58.08	64.8	67.5
Thermodynamic parameters				
		Nd^{+3}	Tb^{+3}	Dy^{+3}
	Temperature (°C)			
	25	0.702	0.853	0.925
K_d	35	0.869	1.128	1.244
	45	1.154	1.534	1.728
ΔH° (kJ/mol)		20.66	24.40	25.97
ΔS° (kJ/mol K)		0.065	0.079	0.085
	Temperature (°C)			

	25	0.877	0.394	0.193
ΔG° (kJ/mol)	35	0.359	-0.308	-0.559
	45	-0.861	-1.131	-1.446

Fig. 1. ^{1}H NMR of the monomer.

Fig. 2. ^{13}C NMR of the monomer.

Fig. 3. ^{1}H NMR of the polymer.

Fig. 4. (A) N_2 adsorption−desorption isotherm and (B) pore size distributions of the synthesized P(PTA).

Fig. 5. (A) XRD pattern of $Ni_{0.2}Zn_{0.2}Fe_{2.6}O_4$ nanopartciles; Photo of $Ni_{0.2}Zn_{0.2}Fe_{2.6}O_4$ nanoparticles (B) before drying and (C) in the solution under magnetic field after drying.

Fig. 6. FE-SEM images of (A) $Ni_{0.2}Zn_{0.2}Fe_{2.6}O_4$ and (B) CMC/P(PTA)/$Ni_{0.2}Zn_{0.2}Fe_{2.6}O_4$.

Fig. 7. FT-IR spectra of (A) $Ni_{0.2}Zn_{0.2}Fe_{2.6}O_4$, (B) P(PTA), (C) CMC, and (D) CMC/P(PTA)/$Ni_{0.2}Zn_{0.2}Fe_{2.6}O_4$.

Fig. 8. EDX spectra of (A) $Ni_{0.2}Zn_{0.2}Fe_{2.6}O_4$ and (B) CMC/P(PTA)/$Ni_{0.2}Zn_{0.2}Fe_{2.6}O_4$.

Fig. 9. TGA/DTGA curves of (A) P(PTA) and (B) CMC/P(PTA)/$Ni_{0.2}Zn_{0.2}Fe_{2.6}O_4$.

Fig. 10. Magnetization curves of (A) $Ni_{0.2}Zn_{0.2}Fe_{2.6}O_4$ and (B) CMC/P(PTA)/$Ni_{0.2}Zn_{0.2}Fe_{2.6}O_4$; (C) Magnetic separation of the ions-loaded adsorbent.

Fig. 11. Effects of (A) pH, (B) contact time, (C) adsorbent dosage, and (D) initial concentration on the adsorption of the ions.

Fig. 12. (A) Effect of ionic strength on the adsorption of the ions, (B) Ln K_d versus 1/T for calculation of enthalpy and entropy changes, (C) Reusability of the CMC/ P(PTA)/$Ni_{0.2}Zn_{0.2}Fe_{2.6}O_4$ for adsorption of the ions, and (D) EDX spectrum of the CMC/ P(PTA)/$Ni_{0.2}Zn_{0.2}Fe_{2.6}O_4$ after adsorption of the ions.

Declaration of competing interest

The authors declare that there is no conflict of interest regarding the publication of this article.

Credit author statement

Hamedreza Javadian: Investigation, Acquisition of data, Analysis and/or interpretation of data, Drafting the manuscript and Revising the manuscript. **Montsserat Ruiz**: Acquisition of data and Supervision. **Mehdi Taghavi**: Experimental, Acquisition of data, Analysis and/or interpretation of data. **Ana Maria Sastre**: Conceptualization and supervision.

Highlights

- The novel biodegradable poly(pyrimidine-thiophene-amide) P(PTA) was synthesized.
- NMR analysis confirmed that the P(PTA) was synthesized successfully.
- The magnetic carboxymethyl chitosan/P(PTA) was prepared by the gelation method.
- The saturation magnetization value of the bionanocomposite was 14.88 emu/g.
- Freundlich model fitted the adsorption equilibrium data of Nd^{+3}, Tb^{+3}, and Dy^{+3}.

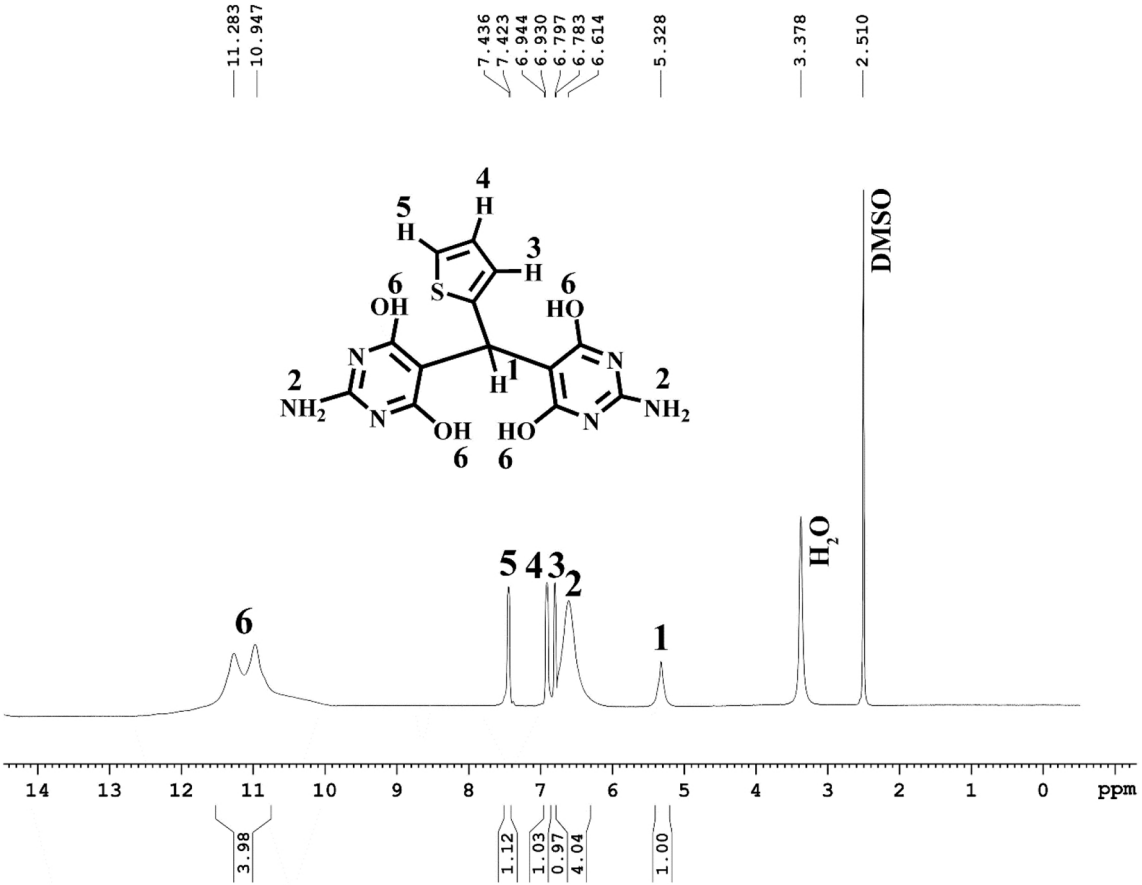
11.283
10.947
7.436
7.423
6.944
6.930
6.797
6.783
6.614
5.328
3.378
2.510
DMSO
H2O
6
5 4 3 2
1
14 13 12 11 10 9 8 7 6 5 4 3 2 1 0 ppm
3.98
1.12
1.03
0.97
4.04
1.00

Figure 1

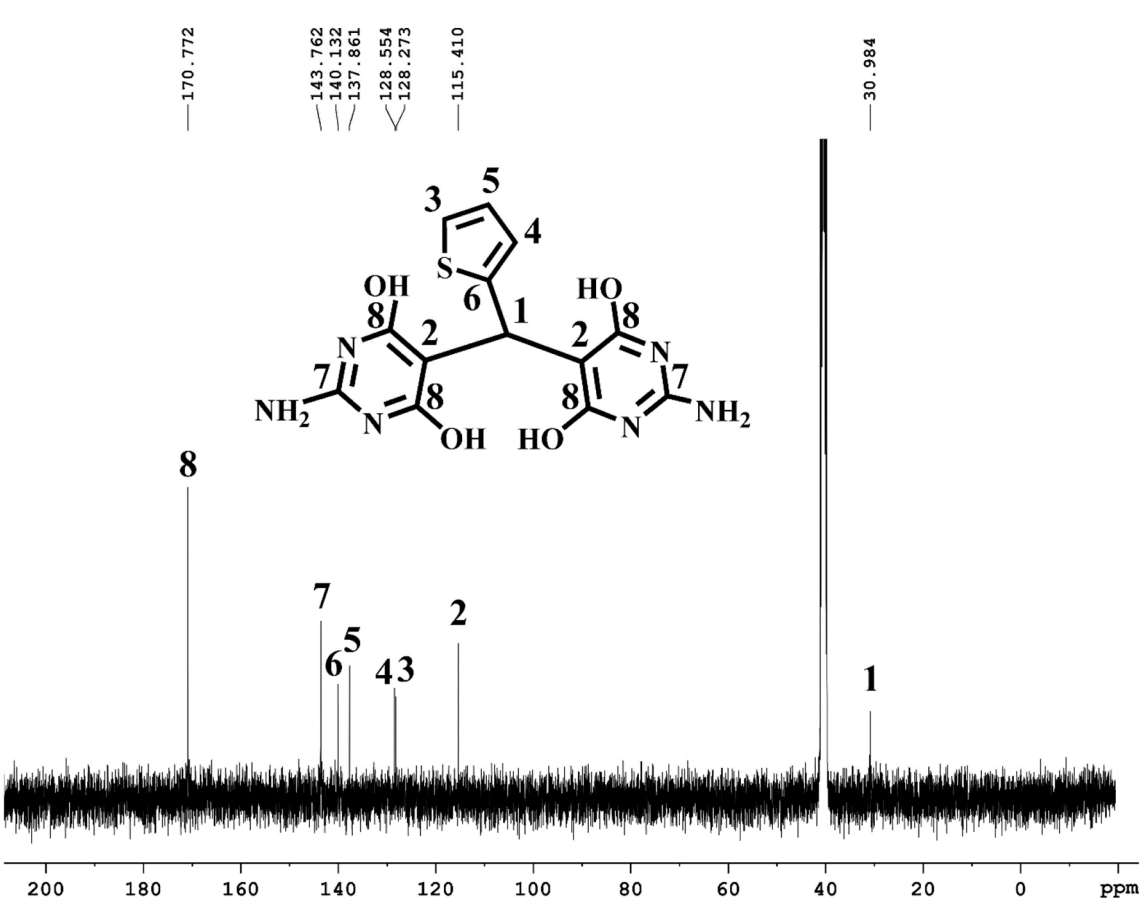
170.772
143.762
140.132
137.861
128.554
128.273
115.410
30.984
OH
HO
NH2
NH2
OH
HO
8
7
6
5
4
3
2
1
200
180
160
140
120
100
80
60
40
20
0
ppm

Figure 2

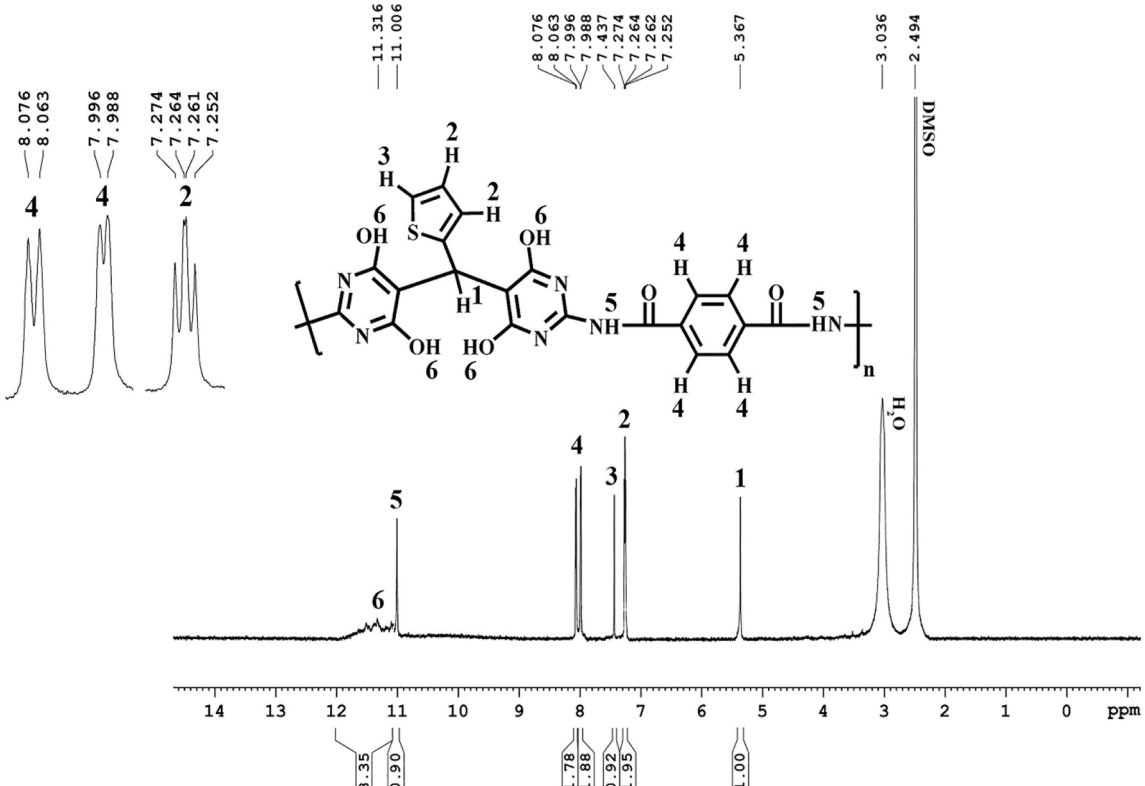
11.316
11.006
8.076
8.063
7.996
7.988
7.437
7.274
7.264
7.262
7.252
5.367
3.036
2.494
DMSO
H2O
8.076
8.063
7.996
7.988
7.274
7.264
7.261
7.252
4
4
2
14
13
12
11
10
9
8
7
6
5
4
3
2
1
0
ppm
3.35
0.90
1.78
1.88
0.92
1.95
1.00

Figure 3

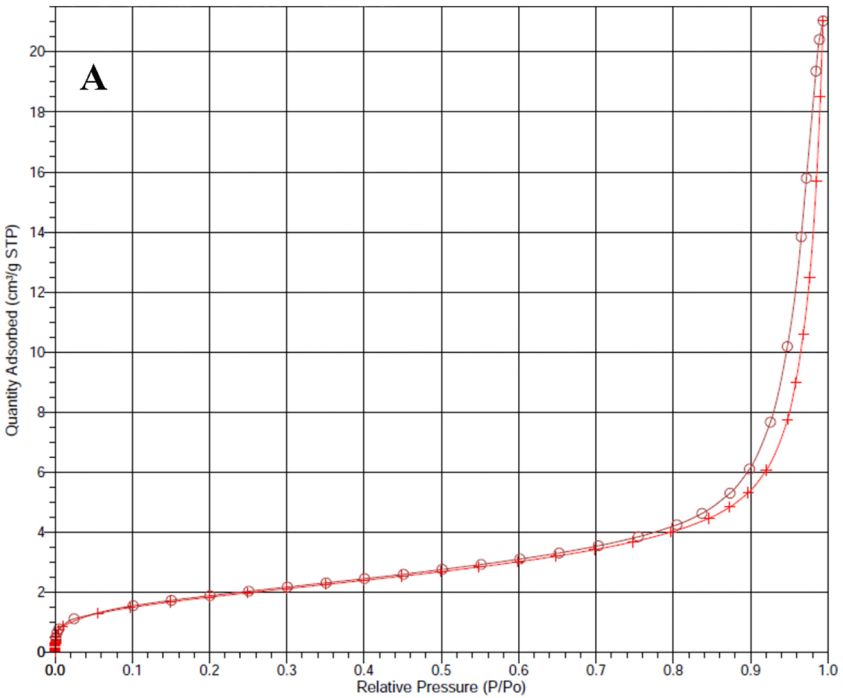
A
Quantity Adsorbed (cm³/g STP)
Relative Pressure (P/Po)
0.0
0.1
0.2
0.3
0.4
0.5
0.6
0.7
0.8
0.9
1.0
0
2
4
6
8
10
12
14
16
18
20

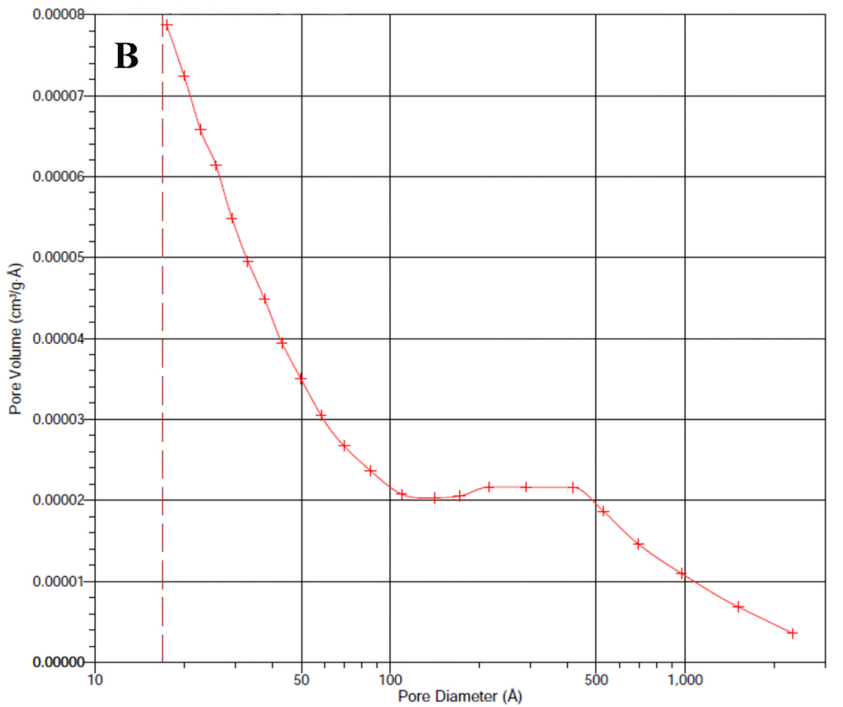
B
Pore Volume (cm³/g Å)
Pore Diameter (Å)
0.00000
0.00001
0.00002
0.00003
0.00004
0.00005
0.00006
0.00007
0.00008
10
50
100
500
1,000

Figure 4

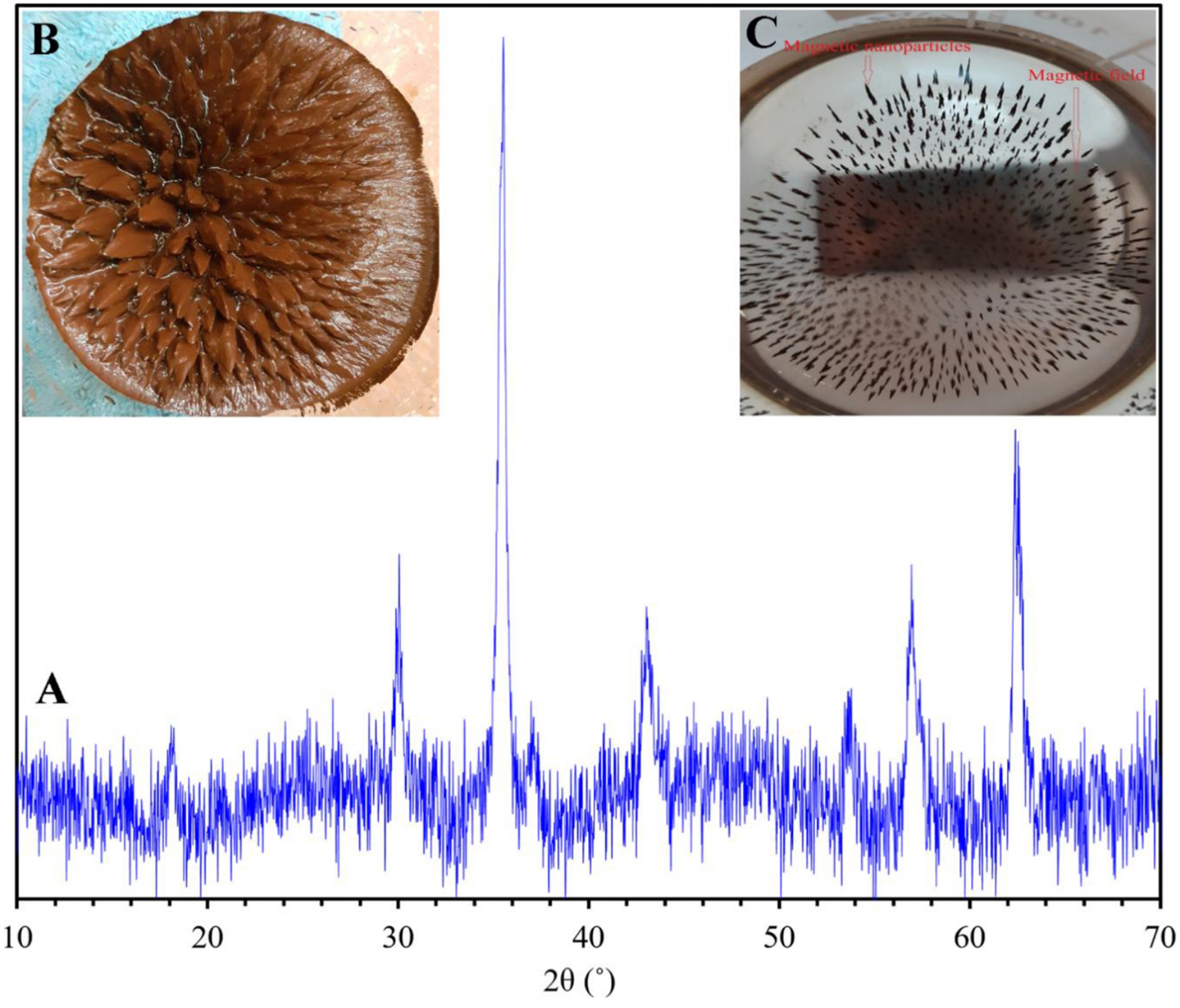
B
C
Magnetic nanoparticles
Magnetic field
A
10
20
30
40
50
60
70
2θ (°)

Figure 5

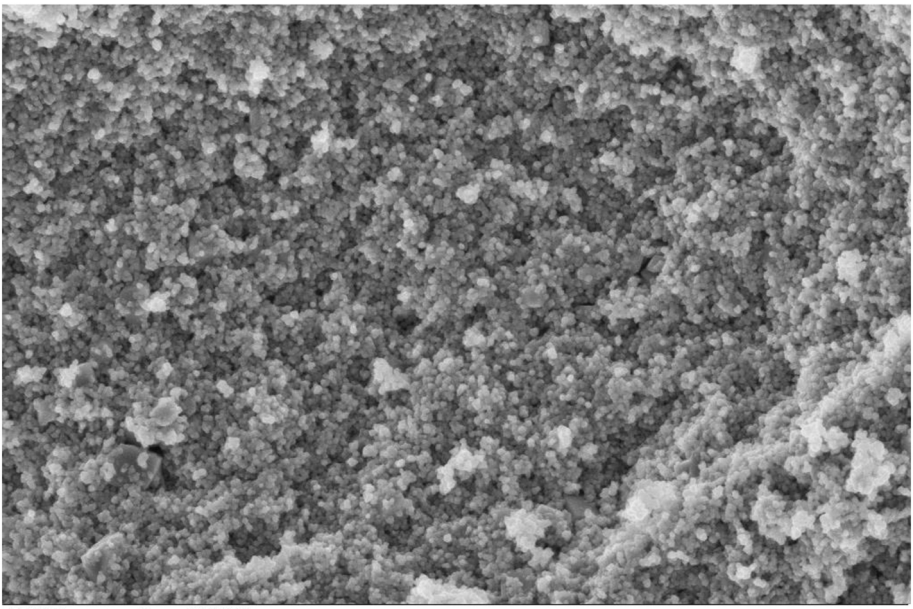
200 nm
Mag = 40.75 K X
WD = 4.5 mm
EHT = 5.00 kV
A

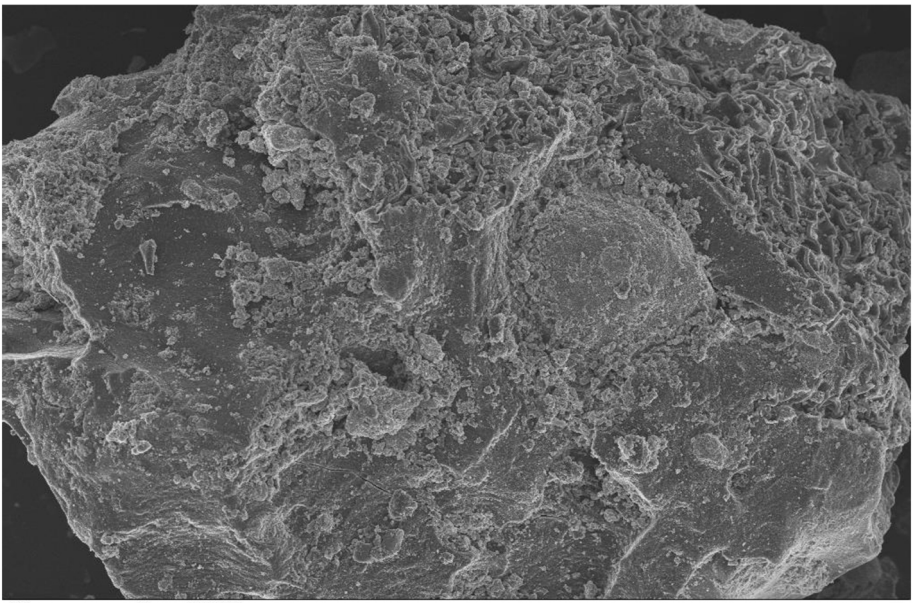
10 µm
Mag = 2.05 K X
WD = 3.8 mm
EHT = 5.00 kV
B

Figure 6

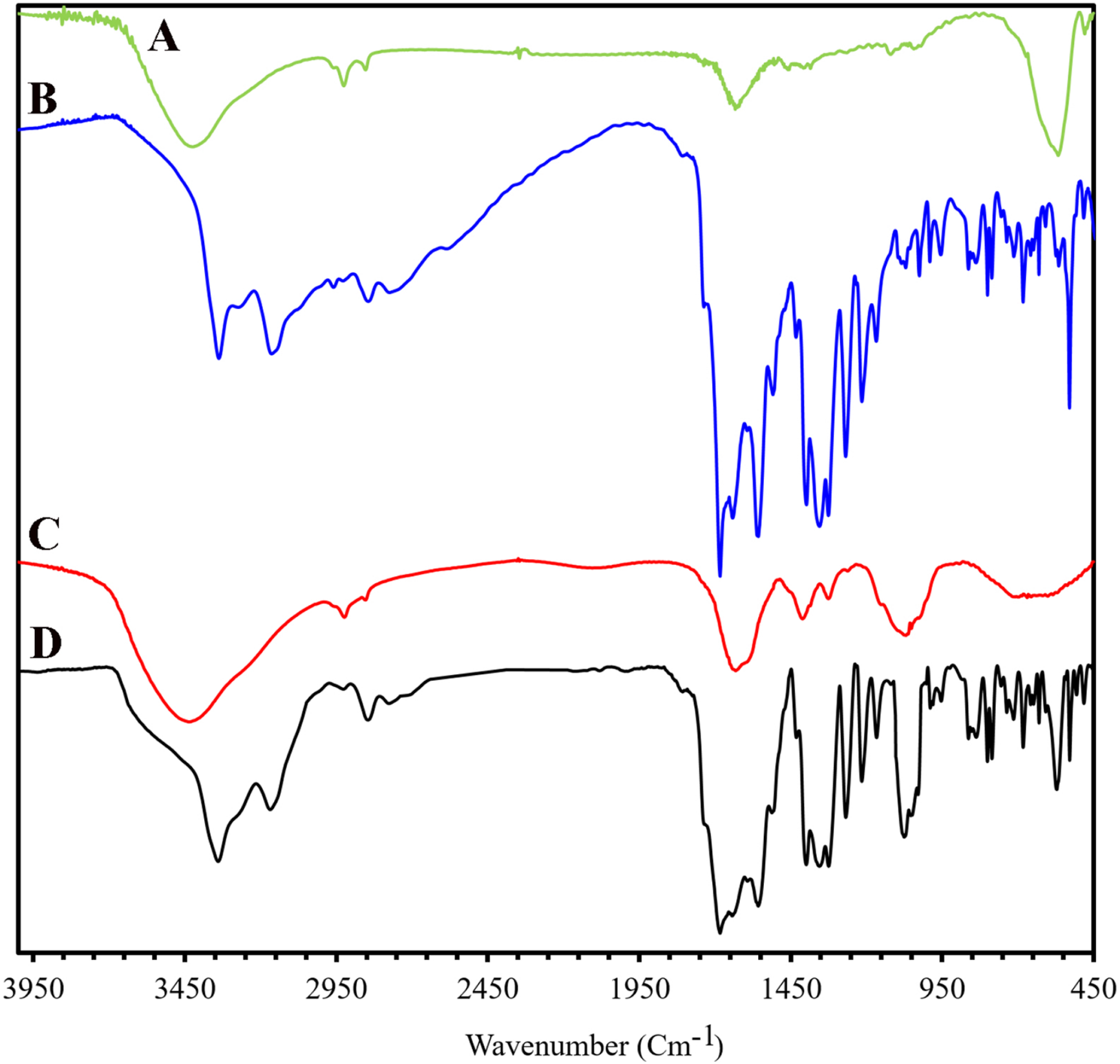

Figure 7

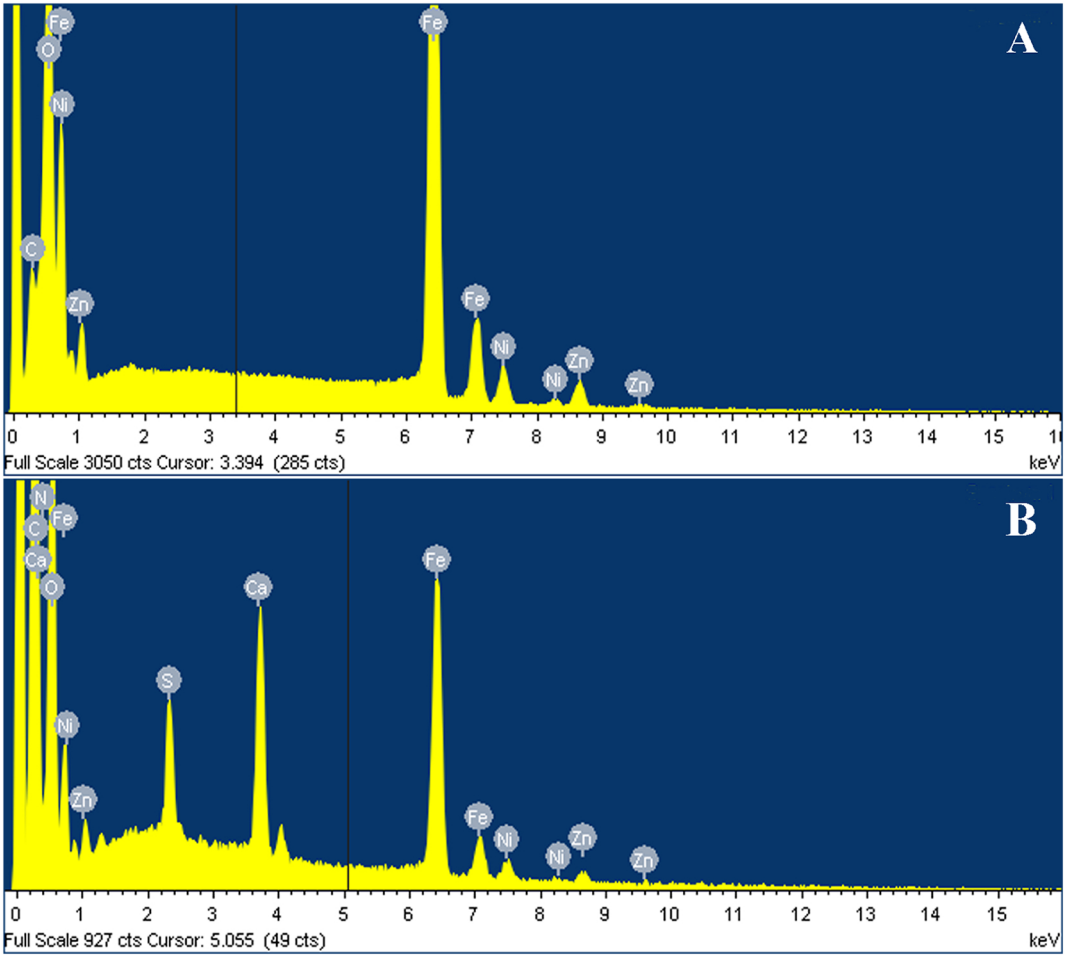
A
Fe
O
Ni
C
Zn
Fe
Fe
Ni
Zn
Ni
Zn
0 1 2 3 4 5 6 7 8 9 10 11 12 13 14 15
Full Scale 3050 cts Cursor: 3.394 (285 cts)
keV
B
N
C
Fe
Ca
O
Ca
Fe
S
Ni
Zn
Fe
Ni
Ni
Zn
Zn
0 1 2 3 4 5 6 7 8 9 10 11 12 13 14 15
Full Scale 927 cts Cursor: 5.055 (49 cts)
keV

Figure 8

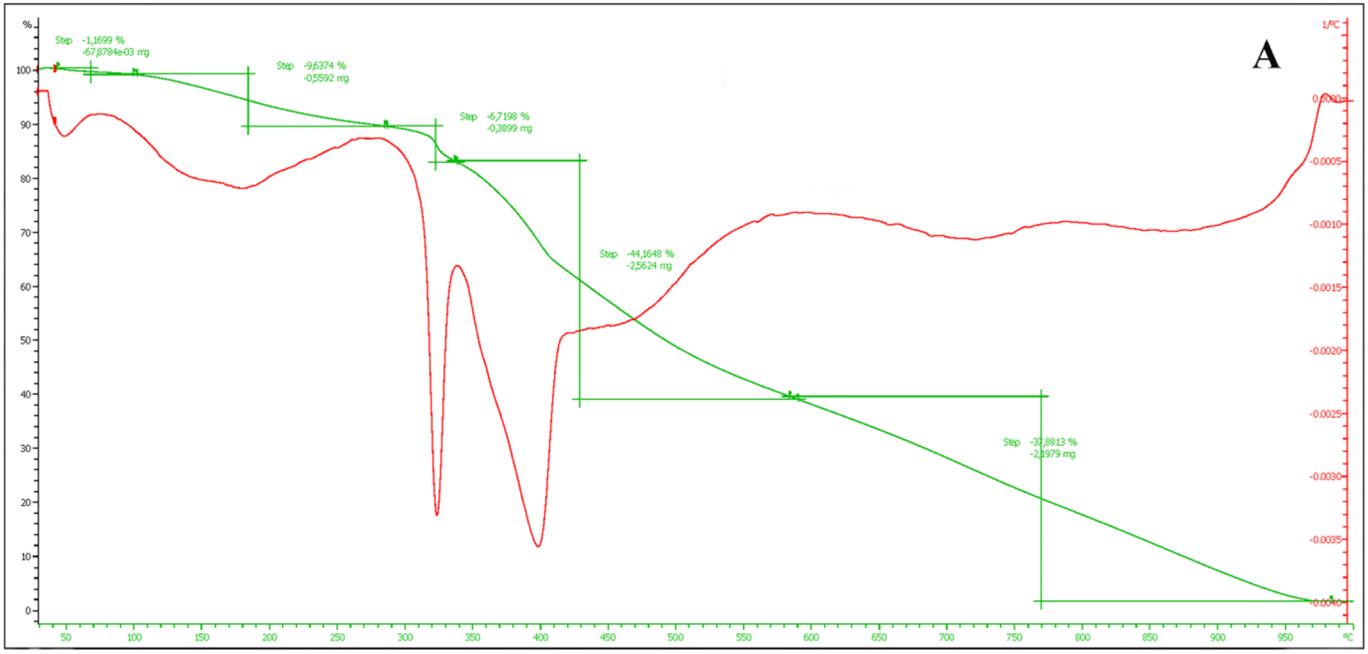
A
Step -1,1699 %
-67,8784e-03 mg
Step -9,6374 %
-0,5592 mg
Step -6,7198 %
-0,3899 mg
Step -44,1648 %
-2,5624 mg
Step -37,8813 %
-2,1979 mg
%
1/°C
°C

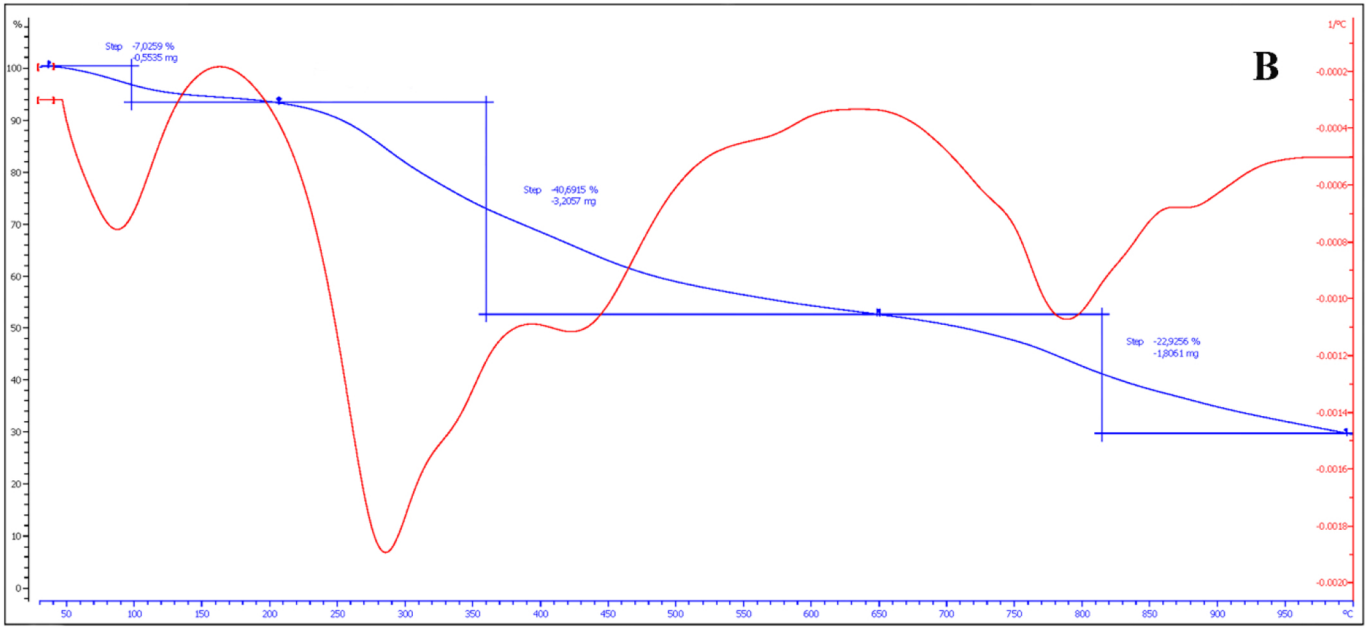
B
Step -7,0259 %
-0,5535 mg
Step -40,6915 %
-3,2057 mg
Step -22,9256 %
-1,8061 mg
%
1/°C
°C

Figure 9

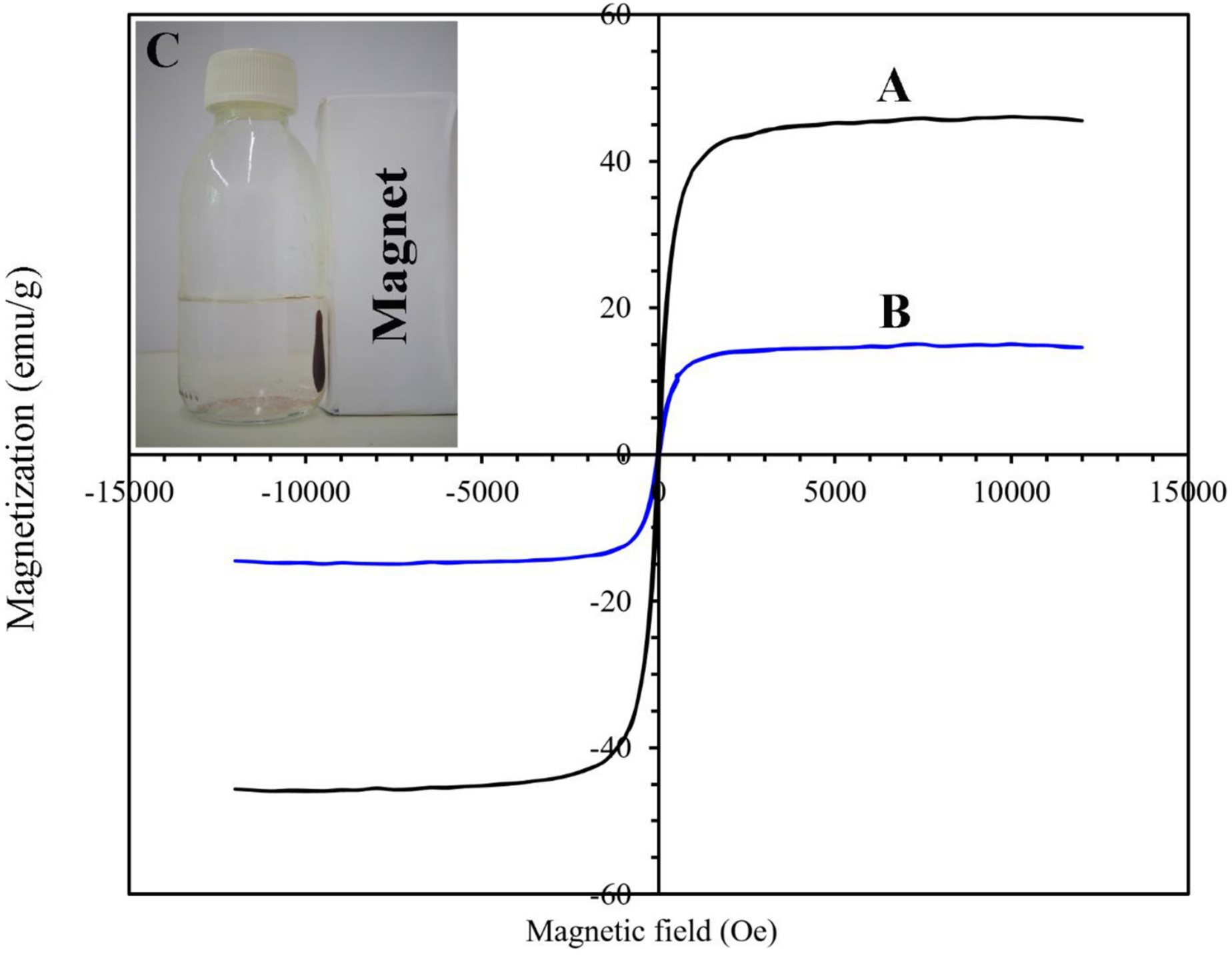
C
Magnet
A
B
60
40
20
0
-20
-40
-60
-15000
-10000
-5000
5000
10000
15000
Magnetization (emu/g)
Magnetic field (Oe)

Figure 10

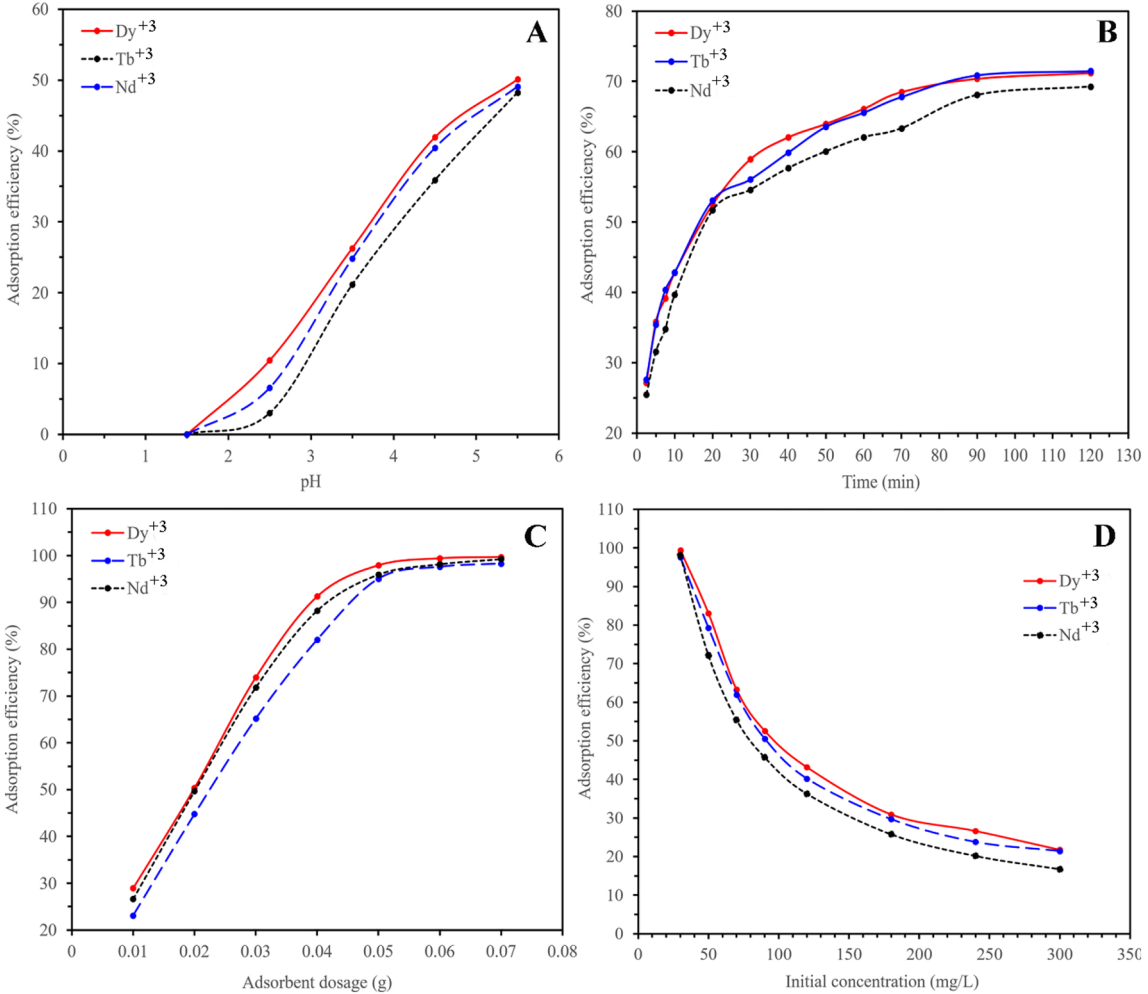
A
Dy+3
Tb+3
Nd+3
Adsorption efficiency (%)
pH
B
Time (min)
C
Adsorbent dosage (g)
D
Initial concentration (mg/L)

Figure 11

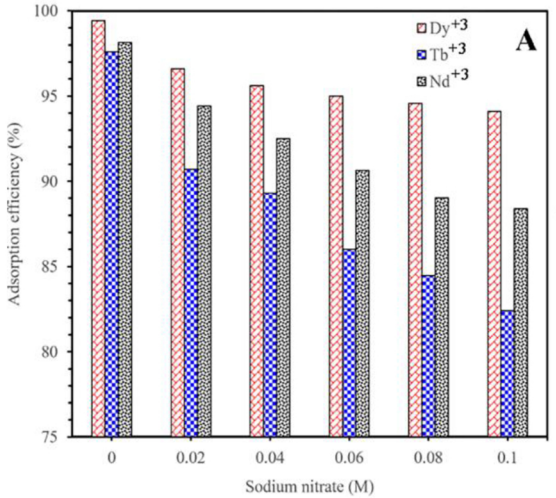
A
Dy+3
Tb+3
Nd+3
Adsorption efficiency (%)
Sodium nitrate (M)
100
95
90
85
80
75
0
0.02
0.04
0.06
0.08
0.1

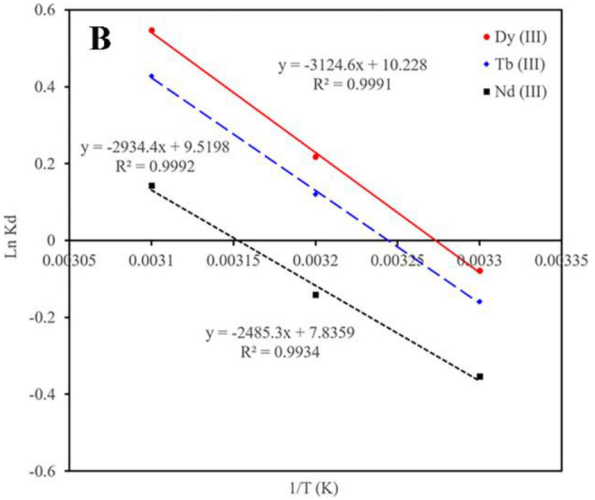
B
Dy (III)
Tb (III)
Nd (III)
y = -3124.6x + 10.228
R² = 0.9991
y = -2934.4x + 9.5198
R² = 0.9992
y = -2485.3x + 7.8359
R² = 0.9934
Ln Kd
1/T (K)
0.6
0.4
0.2
0
-0.2
-0.4
-0.6
0.00305
0.0031
0.00315
0.0032
0.00325
0.0033
0.00335

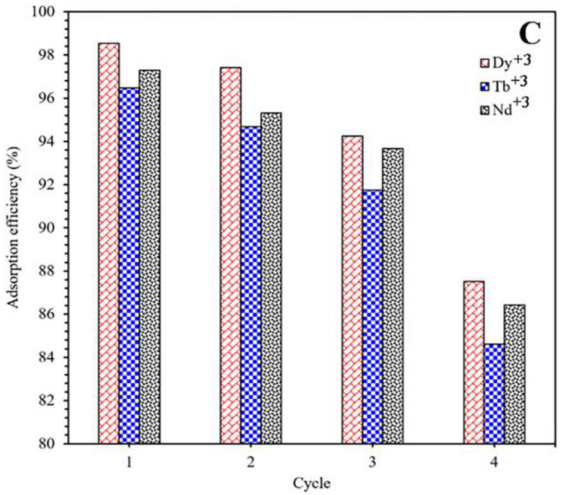
C
Dy+3
Tb+3
Nd+3
Adsorption efficiency (%)
Cycle
100
98
96
94
92
90
88
86
84
82
80
1
2
3
4

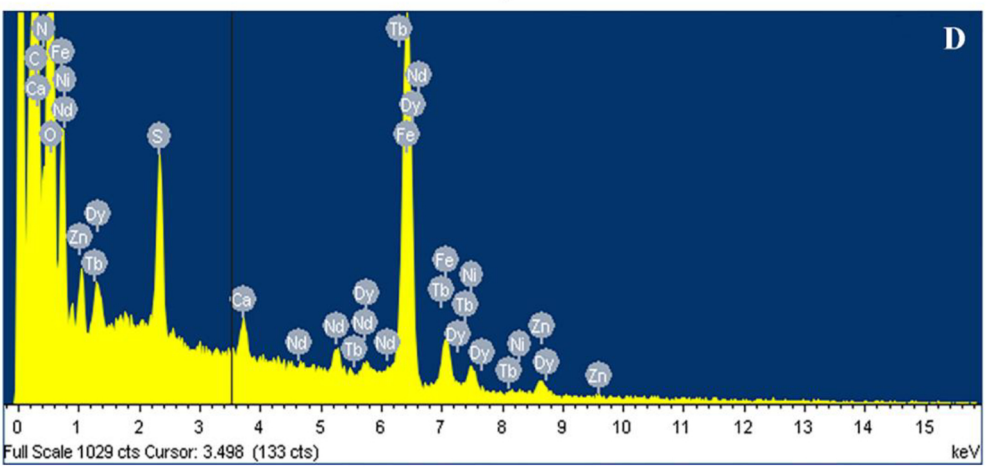
D
N
C
Fe
Ca
Ni
Nd
O
S
Dy
Zn
Tb
Ca
Nd
Dy
Nd
Nd
Tb
Nd
Tb
Nd
Dy
Fe
Fe
Tb
Ni
Tb
Dy
Dy
Ni
Tb
Zn
Dy
Zn
0
1
2
3
4
5
6
7
8
9
10
11
12
13
14
15
Full Scale 1029 cts Cursor: 3.498 (133 cts)
keV

Figure 12